

Segmenting Low-Contrast XCTs of Concretes: An Unsupervised Approach

Kaustav Das^a, Gaston Rauchs^b, Jan Sýkora^a, Anna Kučerová^a

^a*Department of Mechanics, Faculty of Civil Engineering, Czech Technical University in Prague, Thákurova 7, 166 29 Prague 6, Czech Republic*

^b*Structural Composites Unit, Luxembourg Institute of Science and Technology (LIST), 5 avenue des Hauts-Fourneaux L-4362 Esch-sur-Alzette, Luxembourg*

Abstract

This work tests a self-annotation-based unsupervised methodology for training a convolutional neural network (CNN) model for semantic segmentation of X-ray computed tomography (XCT) scans of concretes. Concrete poses a unique challenge for XCT imaging due to similar X-ray attenuation coefficients of aggregates and mortar, resulting in low-contrast between the two phases in the ensuing images. While CNN-based models are a proven technique for semantic segmentation in such challenging cases, they typically require labeled training data, which is often unavailable for new datasets or are costly to obtain. To counter that limitation, a self-annotation technique is used here which leverages superpixel algorithms to identify perceptually similar local regions in an image and relates them to the global context in the image by utilizing the receptive field of a CNN-based model. This enables the model to learn a global-local relationship in the images and enables identification of semantically similar structures. We therefore present the performance of the unsupervised training methodology on our XCT datasets and discuss potential avenues for further improvements.

Keywords: X-ray Computed Tomography (XCT), Concrete, Unsupervised Semantic Segmentation, Convolutional Neural Network (CNN)

1. Introduction

X-ray Computed Tomography (XCT) has garnered substantial interest in experimental mechanics due to its ability to provide information about the internal structure of materials in a non-contact and non-invasive manner. The possibility of extracting detailed morphological information of materials has resulted in its wide adoption in the inspection of multi-phase materials such as composites to study both their internal morphological heterogeneity and defects [75, 51]. Furthermore, subsequent developments in *in-situ* XCT devices now allow observation of materials under loading and enable application of full-field measurement techniques such as digital volume correlation (DVC) [28, 7, 80].

In a wider context, having information about a material's internal morphology and the related property metrics can allow for application of *microstructure sensitive design* methodologies [20] to facilitate design of materials with internal structures tailored for achieving target performance. This is further enabled by the emergence of powerful computational tools both in terms of hardware and software algorithms that can handle large amounts of data, thereby, motivating the use of high-throughput computational methodologies for development of new materials by enabling targeted experiments [16]. Demonstration of such methodologies are seen in the recent emergence of concepts such as digital twins of materials [32], which are conceptualized as highly detailed digital representations of materials, where specialized morphological characterization tools [8] are among key enablers.

In the present use case of concretes, it is recognized that morphological heterogeneities play an important role in their overall behaviour under various loading conditions. Morphology dependence is observed in phenomenon such as drying rate and associated shrinkage and cracks [6, 19], compressive strength [48], interface properties [50, 56], porosity dependent strength [41] among others. In most use cases involving

*Corresponding author. Tel.: +420-2-2435-4375; fax +420-2-2431-0775
Email address: anna.kucerova@cvut.cz (Anna Kučerová)

analysis of concrete in a multi-scale setting, concretes are generally separated into three different phases namely: *aggregates*, *mortar* and *voids* which in the form of cracks and porosity [65]. Although *interfacial transition zones* (ITZ) [62] is also often considered as an additional phase for analysis, but they dependent on the aggregates themselves. Nevertheless, works that analyse concretes by incorporating such morphological features at small material scales still rely on simplified geometric representation of each phase such as ellipses or polygons [29, 24, 49]. For more information one may also refer to the review on modeling of concrete aggregates [58].

Although, XCTs provide rich information about material internal structure, it is not feasible to directly use the obtained grayscale images for subsequent analysis. In particular, the images require use of semantic segmentation tool for partitioning the domain into distinct, non-overlapping regions, with each region representing one of the material phases. Such tools are therefore fundamental for further morphology-based material analysis. However, segmentation of concrete XCT images is particularly challenging because aggregates and mortar have similar X-ray attenuation coefficients, making it difficult to distinguish between them in the XCT images because of their similar grayscale intensity [68, 71]. Some attempts have been made to improve the discernibility of phases through the use of contrast enhancers during concrete mixing [11]. This approach, nevertheless, requires preparation of new test samples with additional additives exclusively for the purpose of tomography and brings additional overheads. Another approach to overcome this limitation involved a study on the use of X-ray tomography and neutron tomography in conjunction to improve the contrast between phases [37]. For more details regarding X-ray tomography one may refer to [10] and for neutron tomography one may refer to [82]. Nevertheless, in most practical cases, only one type of tomography device is readily available.

With several existing works relying on heuristic-based morphology operations for tomographic image segmentation [83, 36], pixel intensity thresholding-based approaches [45, 68, 65, 77] or K-means clustering and level set-based methods [55, 13] etc, all of which primarily consider local image information such as pixel intensity values, there remains a substantial gap in research effort on the development of high-throughput techniques to obtain such domain partitioning of acceptable accuracy that also consider their spatial context and is tailored to the particular use case of tomographic images of concretes. This, therefore, calls for the development of semantic segmentation technique that relies on a single tomography imaging process without any additional overhead associated with creating concrete samples with additives exclusively for the purpose of obtaining tomographic images.

Image segmentation is a much studied topic in the field of computer vision and has seen a substantial amount of progress since the emergence of deep convolutional neural networks (CNN) [42, 43] facilitated by gradient-based optimization through the use of efficient backpropagation algorithms [60]. In the particular case of concretes, image segmentation has primarily been applied to two areas, namely: for detection of cracks in concrete structures and for the determination of aggregate distribution. Therefore, image segmentation in concretes is either performed to detect objects of interest i.e. instance segmentation in works such as [2, 79, 72] or to ascertain the morphology of specific features i.e. semantic segmentation for which one may refer to [76, 17, 61, 46, 27, 3, 71]. The aforementioned works primarily rely on supervised image segmentation and are dependent on the availability of annotated (also referred to as labeled) datasets, which are resource intensive to obtain. Semi-supervised methods using bounding-box level annotations have been explored in [63] and combined usage of annotated and un-annotated datasets in [15]. Nevertheless, requirement for some annotated data for application of these techniques remains.

The alternative approach for image segmentation, i.e. unsupervised segmentation, does not rely on the availability of pre-annotated datasets and has seen application only in crack detection in concrete images where the contrast between the two phases is notable [40, 31, 12]. Therefore, the problem of unsupervised semantic segmentation of multiple phases simultaneously in low-contrast X-ray tomography of concrete remains unexplored.

Several unsupervised semantic segmentation approaches have been explored in computer vision, as demonstrated by works such as [26, 78, 34, 38, 14, 53], with varying degrees of success. However, these studies primarily focus on datasets containing everyday objects and place limited emphasis on precisely capturing object boundaries. In contrast, materials science applications require high accuracy, as segmented components must adhere to physical constraints, such as phase volume fractions or limits on size and shape.

In supervised segmentation, each pixel is paired with a fixed target label during training, while in

unsupervised image segmentation a pixel is assigned a set of feasible target labels rather than a specific target label and the model is expected to learn the correct label for any given pixel during training. As a result, any given pixel is often assigned different target labels during training until the model converges. In existing unsupervised semantic segmentation methods, models are trained by defining a set of feasible labels that is often larger than what is possible for a given dataset [34], which can result in similar semantic objects with slight variations to be assigned different class labels. However, such inconsistencies are undesirable in materials engineering, where the set of feasible class labels, such as aggregate, mortar, and porosity in concretes, are typically predefined.

It is therefore necessary to address this gap in research pertaining to the development of a high-throughput techniques for semantic segmentation of concrete tomography images by leveraging the state of the art tools in image segmentation, namely deep convolutional neural networks (CNN), with a particular focus on annotation-free segmentation methods. In this work we therefore adapt the method originally proposed in [34] for our task of segmenting low-contrast XCT images of concrete. The choice of this method was motivated by the relative ease of specifying the desired number of material phases as well as the minimum spatial size of the relevant phases to be identified during training.

In the ensuing text, Section 2 elaborates on the XCT data acquisition procedure and subsequent preprocessing for image segmentation. Section 3 provides a detailed overview of the unsupervised segmentation procedure, followed by Section 4, which describes the implementation. Sections Section 5, Section 6 and Section 7 cover the experiments, postprocessing technique, and evaluation of the segmentation results, respectively. Finally, Section 8 summarizes this work.

2. X-Ray Computed Tomography Data of Concrete Specimens

2.1. X-Ray Tomography Procedures

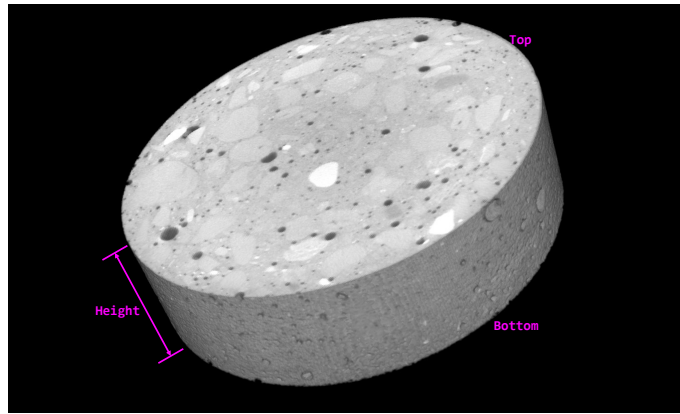


Figure 1: Example of the concrete XCT specimen in 3D.

X-ray computed tomography (XCT) was conducted with the objective to identify three distinct phases in concrete: pores, aggregate, and mortar. To this avail, cylindrical concrete castings, each with a diameter of approximately 94 mm, but of different heights, were used. The composition of the concrete is given in [25]. XCT was performed using an X-Ray MicroCT EasyTom 160 tomograph and Xact reconstruction software (RX Solutions, Chavanod, France). All samples were scanned with a tube voltage of 160 keV and a maximum tube current of $60 \mu\text{A}$. For each specimen, 1440 X-ray projections were recorded during one full rotation of the specimen, using a flat panel detector. The frame rate of the detector ranged between 5 and 6 frames per second, depending on specimen height, with 20 frames averaged per projection. Subsequently, the X-ray projections were processed using Xact reconstruction software to obtain a 3D reconstruction of the specimen, an example of which is presented in Figure 1.

Although a uniform tube voltage and maximum tube current was used while scanning all the cylindrical castings, some issues typical of X-ray computed tomography had to be addressed:

- beam hardening leads to an increase of brightness close to the specimen surface. This effect is reduced by a numerical correction during reconstruction. The correction parameters have to be set manually on an image representative of the specimen, generally in the middle of the specimen. For this reason beam hardening correction is less efficient close to the top and bottom surfaces of the specimen.
- beam diffusion at specimen edges, leading to increased brightness at specimen edges and a halo-effect outside of the surface of the specimen. This effect was strongly reduced by tilting the specimen at an angle of 10° with respect to the rotation axis of the rotation table.
- ring artifacts arise during reconstruction, yielding concentric rings centered with the rotation axis. These rings are attenuated numerically by the reconstruction software via an operator-applied threshold, compromising contrast, and experimentally by the automatic application of small random transversal shifts to the specimen with respect to the rotation axis, different for each image.

In addition, a contrast-enhancing filter was used in the Xact software, resulting in a user-adjusted compromise between sharpness and contrast of the reconstruction. As a result, manual specimen-specific operator interventions introduced noticeable inter-sample variations in the resulting dataset.

The reconstruction was obtained as single channel 16-bit unsigned integer 3D-image stack with voxel values ranging between 0 and 65535 with low values corresponding to the rarer phase such as air or voids and high values corresponding to the denser phases such as mortar and aggregates. Each sample consists of a 3D volumetric representation, comprising a stack of 2D cross-sectional images of the casting, oriented perpendicular to the longitudinal axis of the cylinder. The reconstructions were subsequently re-scaled using bilinear interpolation to achieve a resolution of 1024×1024 per slice, resulting in an approximate voxel size of $93 \mu\text{m}$. For clarity, the term *sample* refers to the XCT reconstruction corresponding to a specific cylindrical casting. The 2D images are referred to as *slices* in this work. Any individual slice or part of it, when considered independently of the sample it originates from, is referred to as an *image*.

It is also to be noted that the neural network architecture employed in the present work processes data as 2D images rather than as a 3D volume, therefore, in the subsequent sections, we refer to each component within a slice as a *pixel*, although it originally corresponds to a *voxel* in the volumetric data.

2.2. Preprocessing

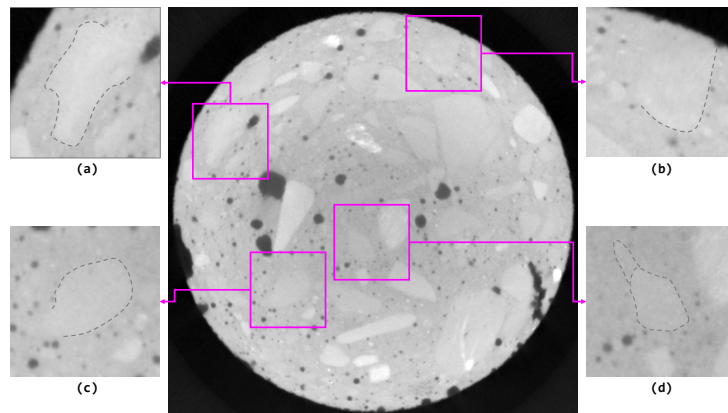


Figure 2: Example of low-contrast regions in an XCT image of concrete. (a)–(c) illustrate aggregates with only part of the aggregate-mortar interface being clearly discernible (indicated by - -). (d) highlights ambiguity in determining the aggregate-mortar interface on a part of the interface.

The similar X-ray attenuation coefficients of aggregates and mortar resulted in low-contrast XCT samples, making it difficult to distinguish between the two materials, as shown in Figure 2. This issue is highlighted in the histograms of voxel intensity of samples, presented in Figure 3, where each sample exhibits two distinct peaks: the left peak corresponds to porosity or air, while the right peak represents the combined aggregate and mortar phase. This overlap complicates the separation of mortar and aggregate

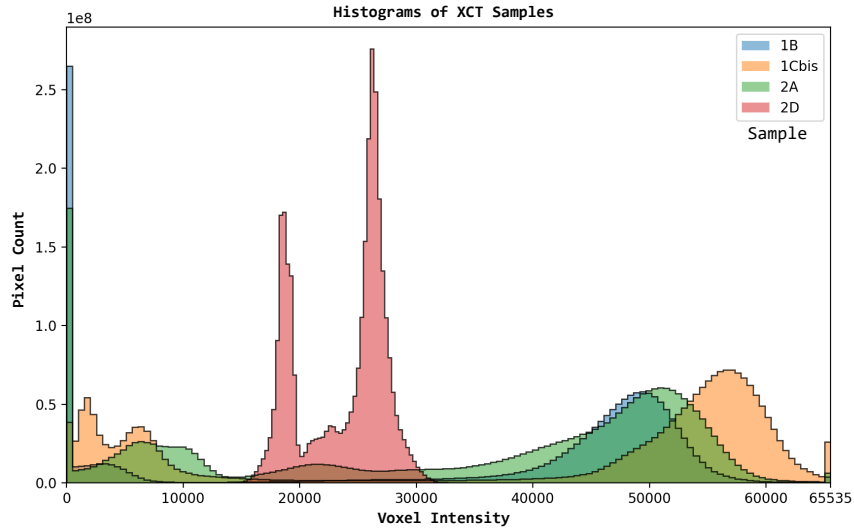


Figure 3: Inter-sample variation of voxel intensity depicted using histograms. For each sample, the peak to the left corresponds to the porosity/air phase, while the peak to the right represents the aggregate and mortar phases in conjunction.

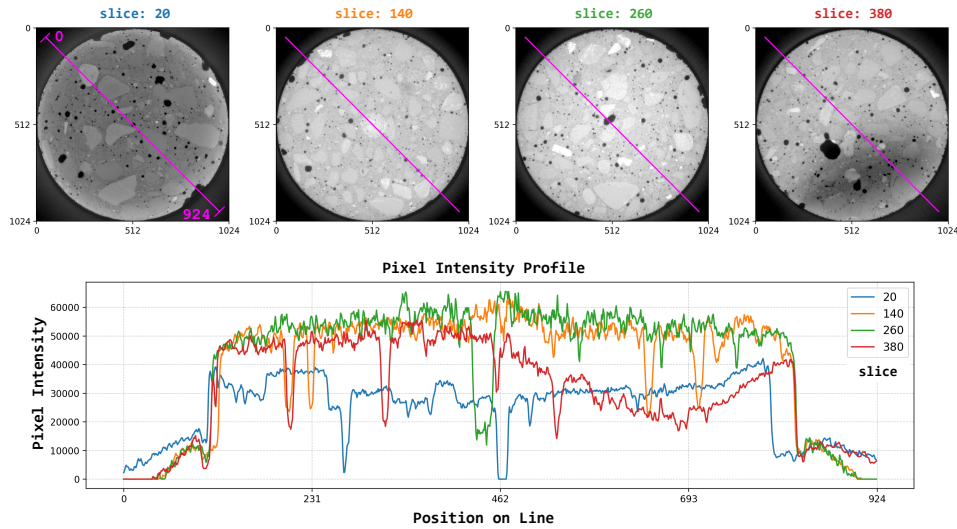


Figure 4: Illustration of variations in pixel values typically observed in all samples shown using selected slices from one sample and their intensity profile across the slice produced using line-intensity profiling. The pixel value along the magenta line in each slice (top row) are plotted below. Slice numbers corresponding to their position along the sample’s height.

phases where ideally, for multiphase materials, one would expect a multimodal distribution with a distinct mode for each phase.

Owing to the inherent heterogeneity of concretes, differences in tomography devices, reconstruction software and operator-specific preferences, it is challenging to eliminate all artifacts and achieve consistent scans across all specimens. Inconsistencies in the concrete XCT dataset include gradual variation of brightness both within slices and between slices of any given sample, a phenomenon observed across all samples. As illustrated in Figure 4 for one sample, the slices towards the top of the cylinder, indicated with a lower number (e.g. slice 20), exhibit lower overall intensity but have relatively high pixel intensities at the periphery of the cylindrical cross-section. As one progresses further along the sample (e.g. slice 140 and 260), overall pixel intensity gradually increases. In the slices towards the bottom of the cylinder (e.g. slice 380), brightness becomes uneven across the cross-section.

Other artifacts include concentric bands of high- and low-intensity rings, loss of detail at the centre of the slices manifesting as blurred regions and a halo-effect around the sample in regions occupied by

air as illustrated in Figure 5(a) - (c) respectively.

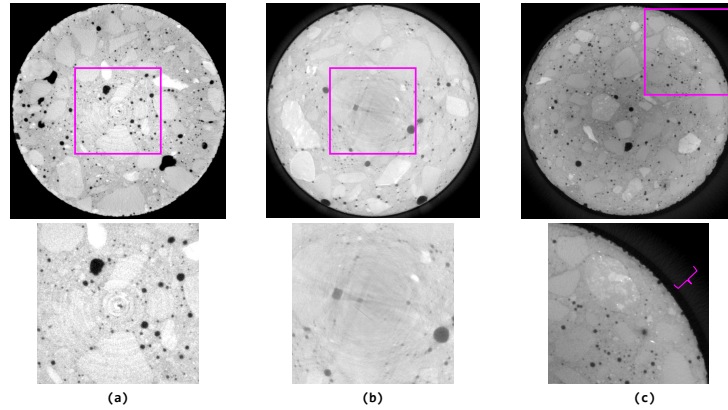


Figure 5: Examples of concentric ring artifact (a), and blurring (b) seen near the centre of the cylinder and halo-effect (c), where regions around the sample show a bright band similar to a halo where no solid material is present.

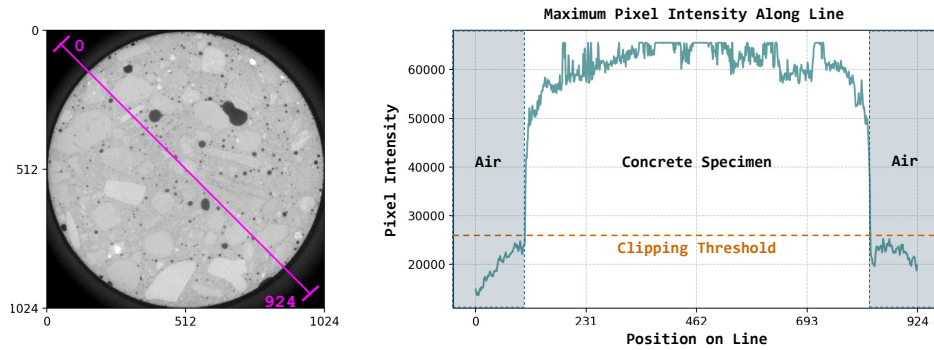


Figure 6: Maximum pixel intensity measured along the magenta line (left image) for the entire sample (along the cylinder height) is plotted (right). Voxels with intensities below the clipping threshold (indicated by - -) are classified as part of the porous phase and are set to zero.

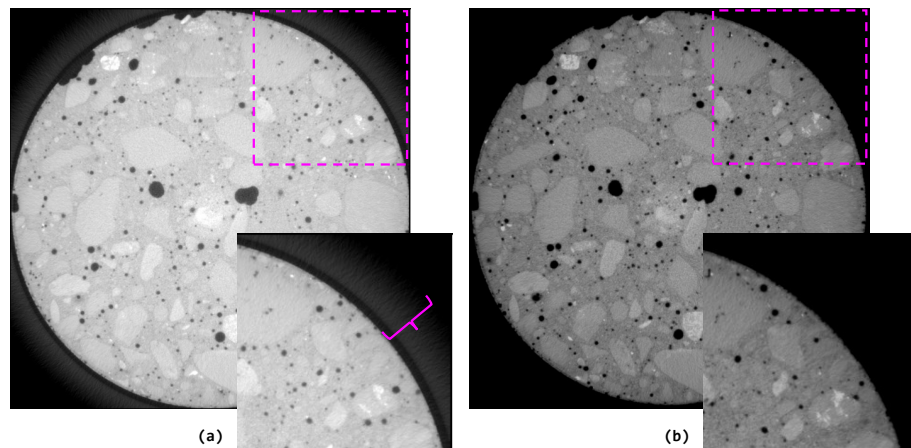


Figure 7: Example of an original image (a) and its preprocessed version (b). Notably, the halo-like artifacts visible in the original are effectively removed after preprocessing. Image (a) is presented in grayscale by setting the grayscale thresholds to the range [0, 65536]. Image (b) is presented by setting the grayscale thresholds to the minimum and maximum values of the sample to which it belongs after standardization.

To attain uniformity in the XCT data, first, the XCT scans were visually inspected and slices exhibiting severe artifacts were discarded such as those exhibiting concentric circle artifacts and loss of detail as in Figure 5(a)-(b), or with uneven brightness across the slice such as slice 380 in Figure 4. The halo-effect was addressed by setting all pixels belonging to the porosity and air phase to zero for each sample to only retain data pertaining to the regions occupied by the solid phase, guided by line-intensity profiles, as illustrated in Figure 6. This was performed individually for each sample and the intensity threshold was manually chosen to be such that non-zero voxel values belonging only to non-solid phase is set to zero.

Finally, for all samples, each slice was individually standardized to have a mean pixel value of 0 and a standard deviation of 1, to mitigate the inter- and intra-sample intensity variations as demonstrated in Figure 3 and Figure 4, respectively. Example of an image obtained after preprocessing is presented in Figure 7. The images thus obtained formed the basis for the training of the segmentation model and subsequent prediction.

3. Unsupervised Semantic Segmentation

3.1. Segmentation Model

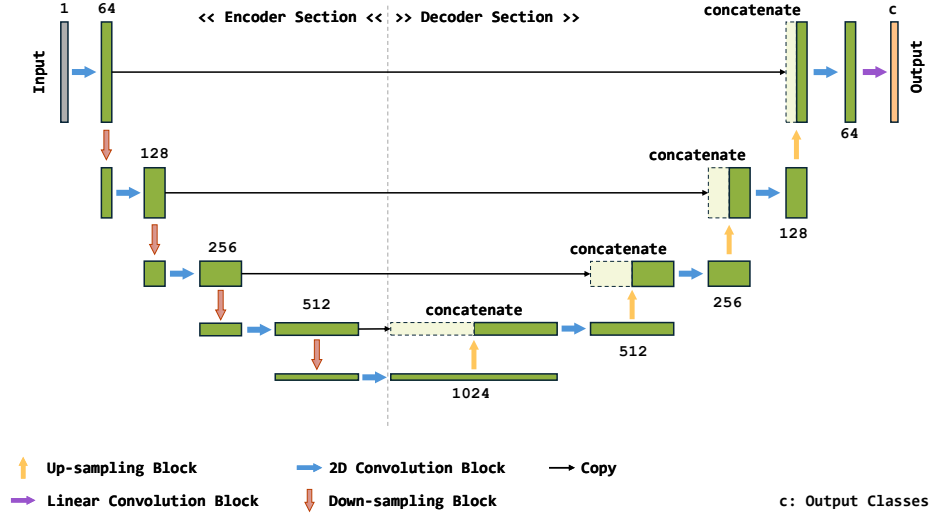


Figure 8: The U-Net model architecture. Green rectangles correspond to feature tensors. Input (grey rectangle) is the grayscale input image. Numbers above or below each rectangle indicate the number of feature channels (or layers or depth) of each tensor, which is also schematically represent the width of the rectangle, whereas the height of each rectangle illustrates the change in spatial dimension (height, width) along the network. Output tensor (in yellow) in this case has $c = 3$, i.e. 3 feature channels, one for each output class.

In contrast to the original approach to unsupervised segmentation proposed in [34], which employs a simple feed-forward CNN architecture [42], the present work adopts a variant of the U-Net architecture [59] (see Figure 8). Originally designed for biomedical image segmentation, particularly CT scans, U-Net has demonstrated superior performance compared to other CNN-based architectures which has led to the development of several variants of it over time [64]. U-Net is essentially composed of an alternating series of convolution, down-sampling, and up-sampling blocks with one linear convolution block at the end, with the convolution operations within each convolution block being central in extracting spatial features from images. This section therefore focuses on concisely outlining the most relevant operations related to the U-Net architecture.

The input to every operation of the U-Net is a tensor $\mathbf{T} = (t_{n,h,w,f}) \in \mathbb{R}^{N \times H \times W \times F}$, where N denotes the number of training samples, so-called batch size (e.g. distinct images, which are the inputs to the very first convolution operation in this model), H and W represent the spatial dimensions - height and width - of the input tensor (e.g. the spatial dimensions of the images in a 2D framework) and F indicates

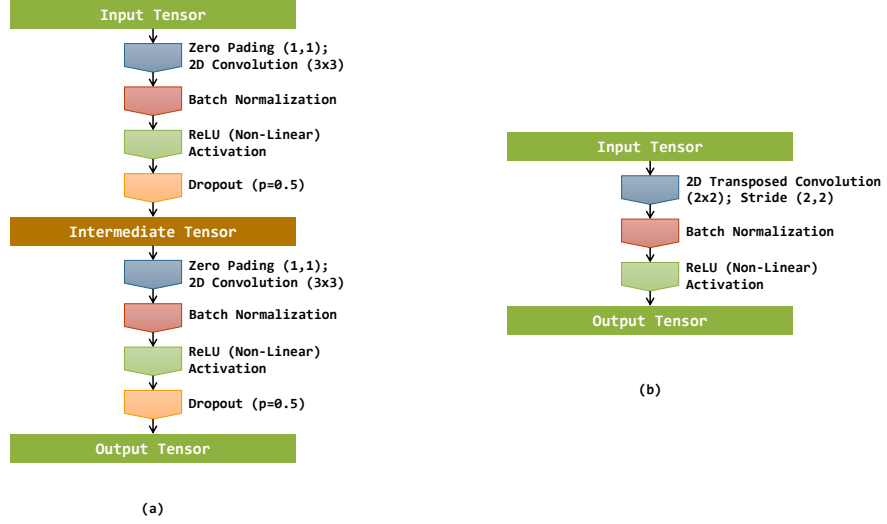


Figure 9: Convolution block (a) and Upsampling block (b). Padding size, kernel size, stride and dropout probability are given in brackets.

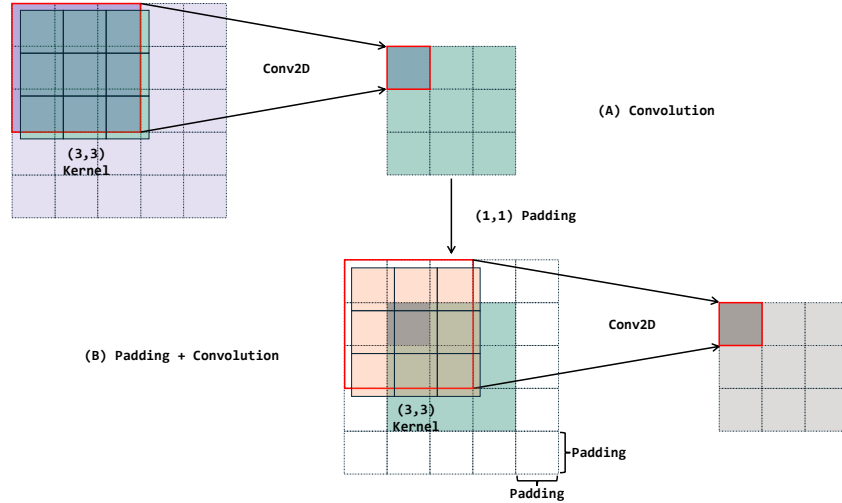


Figure 10: A single-channel input tensor undergoes convolution using kernels of size (3,3) and a stride of (1,1) in (A). Applying the convolution without padding results in a smaller output tensor. By applying appropriate padding prior to convolution, as illustrated in (B), the output tensor maintains the original input size.

the feature dimension (e.g., the number of channels, such as $F = 1$ for grayscale images and $F = 3$ for RGB images).

Each convolution operation used in this model is part of a five-step sequence occurring twice in each convolution block as illustrated in Figure 9(a). As a part of this sequence, the tensors are first expanded along the spatial dimensions using the process of *padding* and specifically, zero-padding in this case, where, s_r rows and s_c columns or 0s are added around the tensor. This ensures that the output tensor of the convolution operation has the same height and width as the input tensor \mathbf{T} , since convolution operation, as used in this work, would otherwise reduce the spatial dimensions. The padded tensor $\mathbf{T}^0 = (t_{n,h,w,f}^0) \in \mathbb{R}^{N \times (H+2s_r) \times (W+2s_c) \times F}$ is thus given as

$$t_{n,h,w,f}^0 = \begin{cases} t_{n,h-s_r,w-s_c,f} & \text{for } s_r < h \leq H + s_r \text{ and } s_c < w \leq W + s_c ; \\ 0 & \text{otherwise} \end{cases} \quad (1)$$

where $s_r \geq 0$ and $s_c \geq 0$.

Zero-padding is followed by the convolution operation. Each convolution operation introduces a unique convolution kernel tensor $\mathbf{K} = (\mathbf{k}_{h,w,f,m}) \in \mathbb{R}^{H_k \times W_k \times F \times M}$ and a unique bias vector $\mathbf{b} = (\mathbf{b}_m) \in \mathbb{R}^M$ with H_k and W_k specifying its height and width and M denoting the desired size of the feature dimension of the output. Given integer valued stride s_H along height and s_W along width, a convolution operation results in an output tensor $\mathbf{T}^c = (\mathbf{t}_{n,h,w,m}^c) \in \mathbb{R}^{N \times H_c \times W_c \times M}$ with all components defined as

$$\mathbf{t}_{n,h,w,m}^c = \sum_{f=1}^F \sum_{q=1}^{H_k} \sum_{r=1}^{W_k} \mathbf{k}_{q,r,f,m} \mathbf{t}_{n,s_H(h-1)+q,s_W(w-1)+r,f}^0 + \mathbf{b}_m \quad (2)$$

and spatial dimensions given as $H_c = (\frac{H+2s_r-H_k}{s_H} + 1)$ and $W_c = (\frac{W+2s_c-W_k}{s_W} + 1)$. The convolution operation is carried out under the constraints $(H + 2s_r - H_k) = as_H$ and $(W + 2s_c - W_k) = bs_W$, where a and b are whole numbers. Strides $s_H \geq 1$ and $s_W \geq 1$ are defined as the number of pixels the convolution kernel travels at a time along height and width respectively. And in the present case, $H_k = W_k = 3$, $s_r = s_c = 1$ and $s_H = s_W = 1$ ensures $H_c = H$ and $W_c = W$. In the encoder section, $M = 64$ in the first convolution block and is doubled in every subsequent convolution block, while in the decoder section, the first convolution block has $M = 512$ and is halved in every subsequent convolution block.

It is to be noted that convolution kernels with either $H_k > 1$ or $W_k > 1$ enable extraction of spatial information from images. As a general rule of thumb, larger kernels allow for information extraction over a larger spatial region, albeit, at a higher computational cost. For more information on convolution operations and CNNs, one may refer to [23, 5]. A visual summary of the convolution process is presented in Figure 10.

In this work, unlike the original U-Net model, convolution operations are followed by *batch-normalization* [30] prior to the application of a non-linear activation function in order to improve training stability and performance. Specifically, given the output of the convolution operation \mathbf{T}^c , batch-normalization is applied to scale all tensor components. This is followed by the application of a non-linear activation function, specifically the *rectified linear unit* (ReLU), which sets all negative tensor components to zero. These two operations in combined form is given as

$$\tilde{\mathbf{t}}_{n,h,w,m}^c = \max(0, \frac{\mathbf{t}_{n,h,w,m}^c - \mu_m^c}{\sigma_m^c} \gamma_m + \beta_m) \quad (3)$$

where $\gamma_m \in \boldsymbol{\gamma} \in \mathbb{R}^M$ and $\beta_m \in \boldsymbol{\beta} \in \mathbb{R}^M$ are learnable parameters of the batch-normalization operation [30] and μ_m^c and $(\sigma_m^c)^2$ denote the mean and variance, respectively, of all components across the batch for the m -th feature computed as

$$\begin{aligned} \mu_m^c &= \frac{1}{NH_cW_c} \sum_{n=1}^N \sum_{h=1}^{H_c} \sum_{w=1}^{W_c} \mathbf{t}_{n,h,w,m}^c \\ (\sigma_m^c)^2 &= \frac{1}{NH_cW_c} \sum_{n=1}^N \sum_{h=1}^{H_c} \sum_{w=1}^{W_c} (\mathbf{t}_{n,h,w,m}^c - \mu_m^c)^2 \end{aligned}$$

thereby resulting in $\tilde{\mathbf{T}}^c = (\tilde{\mathbf{t}}_{n,h,w,m}^c) \in \mathbb{R}^{N \times H_c \times W_c \times M}$.

Furthermore, this work introduces an additional modification to the convolutional block of the original U-Net architecture through the incorporation of *dropout* regularization, aimed at enhancing the model's generalization capabilities [67, 73]. Dropout operates by randomly setting individual tensor components to zero with a probability p_d following a Bernoulli distribution $\mathcal{B}(p_d)$. Hence, for the tensor $\tilde{\mathbf{T}}^c$ and a mask tensor $\mathbf{M} = (\mathbf{m}_{n,h,w,m}) \in \{0, 1\}^{N \times H_c \times W_c \times M}$ with $\mathbf{m}_{n,h,w,m} \sim \mathcal{B}(p_d)$, the result of dropout $\tilde{\mathbf{T}}^{c,d} = \tilde{\mathbf{t}}_{n,h,w,m}^{c,d} \in \mathbb{R}^{N, H_c, W_c, M}$ can be written as

$$\tilde{\mathbf{t}}_{n,h,w,m}^{c,d} = \tilde{\mathbf{t}}_{n,h,w,m}^c \mathbf{m}_{n,h,w,m}. \quad (4)$$

Here, p_d is set to 0.5, which is generally considered optimal [67]. The resulting tensor $\tilde{\mathbf{T}}^{c,d}$ is the output of the sequence of five operations discussed above.

In the encoder section of the model, each convolutional block is followed by a down-sampling operation (red arrows in Figure 8), to reduce the spatial dimensions of the tensors resulting from the preceding convolution block. Unlike the original U-Net architecture, which employs *max-pooling*, this work utilizes *average-pooling* (AvgPool) for down-sampling. This modification showed improvement in segmentation performance during experiments. AvgPool is akin to computing moving average over the components of an input tensor using a convolution operation with a non-trainable moving kernel $\mathbf{K}^1 = (k_{h,w,f,m}^1) \in \{1\}^{H_1 \times W_1 \times F \times F}$ similar to (2) but without an associated bias term. Given an input tensor $\mathbf{T} = t_{n,h,w,f} \in \mathbb{R}^{N,H,W,F}$, this results in $\bar{\mathbf{T}} = (\bar{t}_{n,h,w,f}) \in \mathbb{R}^{N,\bar{H}_A,\bar{W}_A,F}$ with components

$$\bar{t}_{n,h,w,f} = \frac{1}{H_1 W_1} \sum_{q=1}^{H_1} \sum_{r=1}^{W_1} t_{n,s_H(h-1)+q,s_W(w-1)+r,f} \quad (5)$$

and spatial dimensions $\bar{H}_A = (\frac{H-H_1}{s_H} + 1)$ and $\bar{W}_A = (\frac{W-W_1}{s_W} + 1)$. In this case, setting $H_1 = W_1 = 2$ and $s_H = s_W = 2$ leads to $\bar{H}_A = H/2$ and $\bar{W}_A = W/2$.

In the decoder section, each convolution block is preceded by an up-sampling block and a concatenation operation indicated using yellow arrows and black arrows respectively in Figure 8. The up-sampling block, (see Figure 9(b)), consists of a sequence of three operations and is used to increase the spatial dimensions of any given tensor starting with a transposed convolution [81] (see Figure 11(a)-(b)) to counteract the down-sampling.

Formally, each transposed convolution operation introduces a unique transposed convolution kernel tensor $\mathbf{K}^T = (k_{h,w,f,m}^T) \in \mathbb{R}^{H_k^T \times W_k^T \times F \times M}$ and a bias term $\mathbf{b}^T = (b_m^T) \in \mathbb{R}^M$ with H_k^T and W_k^T specifying the height and width of the kernel and M denoting the desired size of the feature dimension of the output. Given an input tensor $\mathbf{T} = t_{n,h,w,f} \in \mathbb{R}^{N \times H \times W \times F}$, components of the transposed convolution output $\mathbf{T}^T = (t_{n,h,w,m}^T) \in \mathbb{R}^{N \times H_T \times W_T \times M}$ are given as

$$t_{n,h,w,m}^T = \sum_{i=1}^H \sum_{j=1}^W \sum_{f=1}^F \sum_{q=1}^{H_k^T} \sum_{r=1}^{W_k^T} t_{n,i,j,f} k_{q,r,f,m}^T \delta_{h,s_H(i-1)+q} \delta_{w,s_W(j-1)+q} + b_m^T. \quad (6)$$

Here $\delta_{i,j}$ is the Kronecker delta. In the present work, $s_H = s_W = 2$ and $H_k^T = W_k^T = 2$ are used in order to obtain $H_T = 2H$ and $W_T = 2W$. For every transposed convolution block the number of output feature dimensions is set at $M = F/2$.

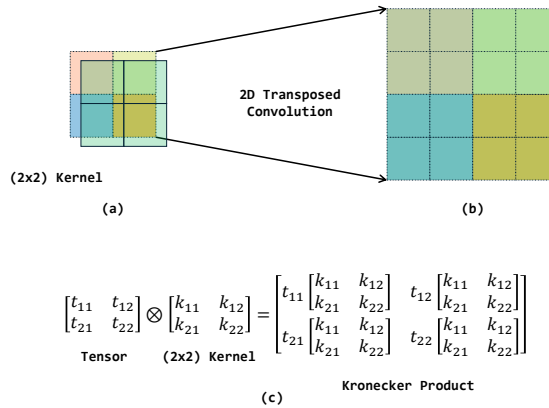


Figure 11: 2D transposed convolution on a single channel input, i.e. $F = 1$ with kernel size $H_k^T = W_k^T = 2$ and stride $s_H = s_W = 2$ resulting in tensor (b) that is twice the size of the input (a). The same can be represented using a Kronecker Product for a case when $s_H = H_k^T$ and $s_W = W_k^T$ individually for each channel and is presented in (c).

In this particular case, where the stride and kernel sizes are equal, transposed convolution operation reduces to a kronecker product between the slices of the input tensor and corresponding slices of the

convolution kernel. To be more specific, given tensor slice $\mathbf{I}_{n,f} \in \mathbb{R}^{H \times W}$ of a given data sample n and feature channel f of \mathbf{T} such that $\mathbf{T} = \{\mathbf{I}_{n,f} | n \in [1, 2, \dots, N], f \in [1, 2, \dots, F]\}$ and kernel slices $\mathbf{K}_{f,m}^T$, for any given input and output feature channel f and m of \mathbf{K}^T respectively, such that $\mathbf{K}^T = \{\mathbf{K}_{f,m}^T | f \in [1, 2, \dots, F], m \in [1, 2, \dots, M]\}$, the result of the transposed convolution becomes $\mathbf{T}^T = \{\mathbf{I}_{n,m}^T\}$, where each tensor slice $\mathbf{I}_{n,m}^T$ is equivalent to the kronecker product $\mathbf{I}_{n,m}^T = \mathbf{I}_{n,f} \otimes \mathbf{K}_{f,m}^T$ (see Figure 11(c)). The transposed convolution operation is followed by batch normalization and a non-linear activation using ReLU, identical to (3). It is worth noting that, instead of transposed convolution, tensors could alternatively be up-sampled using interpolation. However, this configuration was not explored in the present work.

Following the up-sampling block and prior to each convolution operation in the decoder section, at each hierarchical level of the model, the up-sampled tensor is concatenated to the convolution output of equal spatial dimension from the encoder section (black arrows in Figure 8). For any two tensors $\mathbf{T}^A = (t_{n,h,w,m_A}^A) \in \mathbb{R}^{N \times H \times W \times M_A}$, and $\mathbf{T}^B = (t_{n,h,w,m_B}^B) \in \mathbb{R}^{N \times H \times W \times M_B}$, concatenated tensor $\mathbf{T}^C = (t_{n,h,w,m_C}^C) \in \mathbb{R}^{N \times H \times W \times M_A + M_B}$ is given as

$$t_{n,h,w,m_C}^C = \begin{cases} t_{n,h,w,m_C}^A & \text{for } 1 \leq m_C \leq m_A; \\ t_{n,h,w,m_C - m_A}^B & \text{for } m_A < m_C \leq m_A + m_B. \end{cases} \quad (7)$$

The final block of the model is the linear convolution block (purple arrow in Figure 8). This block is composed of a single convolution operation, equivalent to (2), but with $H_k = W_k = 1$, $s_H = s_W = 1$ and $M = 3$ or 4 depending on the experiment. The choice of kernel size and strides preserve the spatial dimension and do not necessitate use of padding prior to convolution. Furthermore, no batch normalization, non-linear activation or dropout is performed in this block.

The U-Net model for semantic segmentation employed in this work is hereafter denoted by \mathcal{U} and represents a mapping between tensors. \mathcal{U} is parameterized by a set of variables collectively referred to as θ , which comprises all the trainable convolution kernels and their corresponding bias terms associated with the convolution and up-sampling blocks of the network and also the trainable parameters associated all the batch-normalization operations. Assuming the entire model has L convolution operations and L^T transposed convolution operations, each with a kernel-bias pair $(\mathbf{K}, \mathbf{b})_i$ and $(\mathbf{K}^T, \mathbf{b}^T)_j$, and $(L + L^T - 1)$ batch-normalization operation, each with a pair of parameter vectors $(\gamma, \beta)_k$, the parameter set θ is formally defined as $\theta = \{(\mathbf{K}, \mathbf{b})_i, (\mathbf{K}^T, \mathbf{b}^T)_j, (\gamma, \beta)_k | i \in [1, 2, \dots, L], j \in [1, 2, \dots, L^T] \text{ and } k \in [1, 2, \dots, L + L^T - 1]\}$. The values of these parameters are initially unknown and are determined during training. Finally, the notation \mathcal{U}_θ is used to refer to the model parameterized with a specific θ .

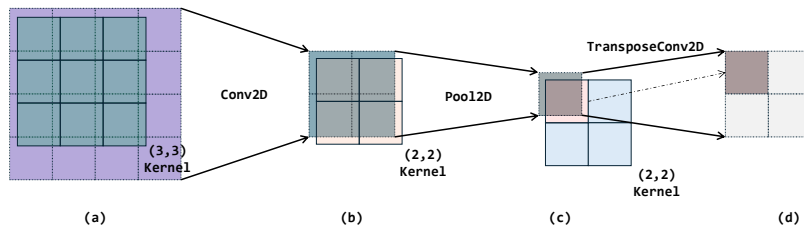


Figure 12: Illustration of a receptive field. The highlighted pixel in (d) is the result of applying a convolution with a (3×3) kernel and stride $(1,1)$ on the input in (a), followed by a pooling operation with a (2×2) kernel in (b), and a transposed convolution using a (2×2) kernel in (c). This pixel in (d) is influenced by a 4×4 region of the original input tensor in (a).

3.2. Model Input

In this work, input to the first convolution operation of \mathcal{U} is a tensor $\mathbf{T} \in \mathbb{R}^{N \times H \times W \times 1}$. Here N indicates the number of images being passed into the model at once and the last dimension of size 1 indicates a single-channel/grayscale image. For convenience \mathbf{T} is hereon defined as a set of images as $\mathbf{T} = \{\mathbf{I}_1, \mathbf{I}_2, \dots, \mathbf{I}_N\}$ where $\mathbf{I}_n = (p_{n,h,w}) \in \mathbb{R}^{H \times W}$ is a digital image composed of pixels $p_{n,h,w}$ [22]. In

the remainder of this section, the analysis is restricted to a single image; hence, the index n has been omitted in favour of readability.

In practice, given the mapping $\mathbf{I} \xrightarrow{\mathcal{U}} \hat{\mathbf{Y}} = (\hat{y}_{h,w,f}) \in \mathbb{R}^{H \times W \times F}$, each output component $\hat{y}_{h,w,f}$ at a given spatial location (h, w) is influenced only by a unique subset of input image components $\mathbf{F}^{(h,w)} = \{p_{i,j}\}_{(h,w)} \subseteq \mathbf{I}$, the so-called *receptive-field* (RF) of a CNN, simplified example of which is illustrated in Figure 12; for more information, one may refer to [70]. An RF is unique to each CNN architecture.

Therefore, to ensure compatibility of the input images with \mathcal{U} , it is required that for any image \mathbf{I} and output component $\hat{y}_{h,w,f}$, there exists a region $\mathbf{F}^{(h,w)} \subseteq \mathbf{I}$ that is compatible with the RF of \mathcal{U} . In the limiting case where the output tensor is spatially collapsed, i.e. $\hat{\mathbf{Y}} \in \mathbb{R}^{1 \times 1 \times F}$, the input must correspond to the receptive field, i.e. $\mathbf{I} = \mathbf{F}^{(1,1)} = \{p_{i,j}\}_{(1,1)}$. Consequently, tensors with spatial dimensions smaller than the receptive field are not supported by \mathcal{U} .

3.3. Supervised Semantic Segmentation

Given a set of discrete variables, here referred to as a set of categorical classes $\mathcal{C} = \{c_1, c_2, c_3, \dots\}$, representing the material phases of interest, the task of *pixel classification* is defined as the problem of assigning to each pixel $p_{h,w}$ of an image \mathbf{I} a class $c_{h,w} \in \mathcal{C}$. *Semantic segmentation* extends this task further to enforce spatial continuity, i.e., locations in close proximity and with similar $\mathbf{F}^{(h,w)}$ are encouraged to have identical labels. As a result, contiguous regions of identically labeled pixels correspond to semantically meaningful structures within the image. In other words, this means that nearby locations with similar $\mathbf{F}^{(h,w)}$ are more likely to belong to the same real-life object.

Therefore, given an image \mathbf{I} , and a model \mathcal{U}_θ with a set of parameters θ , the mapping performed by the model is defined as: $\mathbf{I} \xrightarrow{\mathcal{U}_\theta} \hat{\mathbf{Y}}_\theta = (\hat{y}_{h,w}^\theta) \in \mathbb{R}^{H \times W \times |\mathcal{C}|}$ where $|\mathcal{C}|$ is the number of categorical classes and $\hat{y}_{h,w}^\theta \in \mathbb{R}^{|\mathcal{C}|}$ represents the vector of prediction scores for each categorical class with each score indicating how likely it is for a given $p_{h,w}$ to belong to one of the $|\mathcal{C}|$ categorical classes depending on the corresponding $\mathbf{F}^{(h,w)}$. Generation of correct prediction scores requires an optimal set of parameters θ , which is obtained by minimizing an objective function during training.

Semantic segmentation models for images are usually trained using *cross-entropy* loss \mathcal{L}_{CE} as the objective function. In the case of CNN-based architectures, for every region $\mathbf{F}^{(h,w)}$, crossentropy-loss mandates the existence of a known label $l_{h,w} \in \mathcal{C}$. These labels collectively form the tensor $\mathbf{L} = (l_{h,w}) \in \mathcal{C}^{H \times W}$, known as the labeled image (or annotated image) of \mathbf{I} . For practical reasons, \mathbf{L} is one-hot encoded as $\mathbf{Y}^{01} = (y_{h,w,f}) \in \{0, 1\}^{H \times W \times |\mathcal{C}|}$ with components

$$y_{h,w,f} = \begin{cases} 1 & \text{if } l_{h,w} = c_f \in \mathcal{C} \\ 0 & \text{otherwise} \end{cases} \quad (8)$$

such that $\sum_{f=1}^{|\mathcal{C}|} y_{h,w,f} = 1$. \mathbf{Y}^{01} thus represents the target label for training the segmentation model in a supervised manner. Here, the labeled image imparts semantic supervision to the model outputs and enforces spatial contiguity.

Training is usually performed by iterating over the data multiple times. At any given iteration t , the segmentation model \mathcal{U} is parameterized by the set θ_t specific to that iteration and the model prediction for an image \mathbf{I} is given as $\mathbf{I} \xrightarrow{\mathcal{U}_{\theta_t}} \hat{\mathbf{Y}}_t = (\hat{y}_{h,w,f}^t) \in \mathbb{R}^{H \times W \times |\mathcal{C}|}$ at that iteration. Therefore, for any \mathbf{I} , its model prediction $\hat{\mathbf{Y}}_t$ and the corresponding one-hot encoded target label \mathbf{Y}^{01} , the crossentropy loss at iteration t is defined as

$$\mathcal{L}_{\text{CE}}^t = - \sum_{h=1}^H \sum_{w=1}^W \sum_{f=1}^{|\mathcal{C}|} \log \left(\frac{\exp(\hat{y}_{h,w,f}^t)}{\sum_{f=1}^{|\mathcal{C}|} \exp(\hat{y}_{h,w,f}^t)} \right) y_{h,w,f}. \quad (9)$$

In this case, $y_{h,w,f}$ is fixed for all iterations throughout the training for a given image.

3.4. Self-Annotation and Unsupervised Semantic Segmentation

For any image \mathbf{I} in this case, \mathbf{L} does not exist and is expensive to obtain, necessitating an algorithm to generate the required labels during training. This algorithm must take into account the requirement that nearby pixels with similar global and local context are likely to share the same semantic class. As such, the generated labels must consist of contiguous regions with identically labeled pixels such that each such region forms a semantically meaningful structure.

A key property of CNN-based models is the fact that they are able to partition a given image based on complex information, such as spatial arrangement of objects contained in the receptive field corresponding to each pixel of the output. And therefore, it is possible for the model to identify individual pixels in close proximity, which are otherwise similar in intensity, as different semantic class due to difference in the information contained within the respective receptive fields and vice versa. This is particularly evident in the initial phases of training, as indicated in Figure 13, where, despite the use of identical model parameters for a given image, identically coloured pixels in immediate proximity within each image do not generate correspondingly high score for the identical semantic class relative to the other semantic classes. As such, the parameter set θ of the model if simultaneously trained to associate pixels in close proximity and with similar intensities with identical semantic class, may develop a global-local relationship and learn to associate nearby pixels with similar intensity and global context with the identical semantic class.

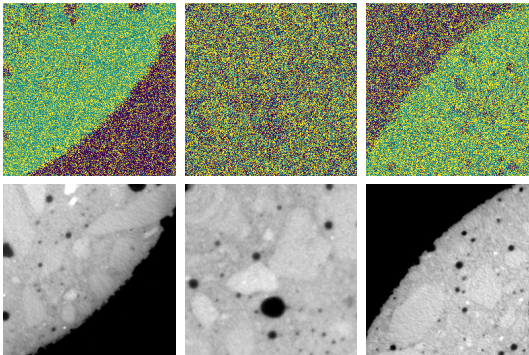


Figure 13: Example of arg max application on the prediction values of three randomly selected training samples in the first training epoch. Each colour is representative of the categorical class with the maximum prediction value.

This necessitates identification of localized regions in an image that, on the account of perceptual similarity, may belong to the same semantic class. To this end, there exists a class of heuristics-based algorithms that are able to identify perceptually similar regions in an image and generate clusters known as *superpixels*. Pixels belonging to these clusters also additionally satisfy the requirement of spatial proximity. Therefore, in this context, we define a set of I superpixels of an image \mathbf{I} as $\{\mathcal{P}_i\}_{i=1}^I$ where each superpixel $\mathcal{P}_i = \{p_{h,w}\}_i$ represents a spatially contiguous, non-empty and non-overlapping region of an image such that $\cup_{i=1}^I \mathcal{P}_i = \mathbf{I}$, with any given superpixel occupying a spatial region $\Omega_{\mathcal{P}_i} = \{(h,w)\}_i$ of an input image. Consequently, the set $\{\Omega_{\mathcal{P}_i}\}_{i=1}^I$ of spatial regions that can be used to associate each pixel in an image to a unique superpixel is hereon termed as *superpixel-map* of an image.

Since superpixel algorithms cluster together regions of perceptual similarity (see Figure 14), the generated superpixels are also able to demarcate boundaries between perceptually distinct regions and therefore, in this application, also enable identification of interface between the constituent phases. This is particularly evident when using the algorithm termed as SLIC [1], which is readily available as part of the image processing library *Scikit-Image* [74]. Therefore, for generation of superpixels in this work, SLIC was chosen, as it outperformed other algorithms including the more recent watershed segmentation technique proposed in [52]. Nevertheless, it must be noted that superpixels are limited to local perceptual similarity and do not identify objects or assign semantic meaning to the regions and therefore do not comprise any information beyond their boundaries.

Hence, in order to obtain automated labels, an assumption is made that given a superpixel \mathcal{P}_i at locations indicated by $\Omega_{\mathcal{P}_i}$ the most frequently occurring class label for the pixels at these locations

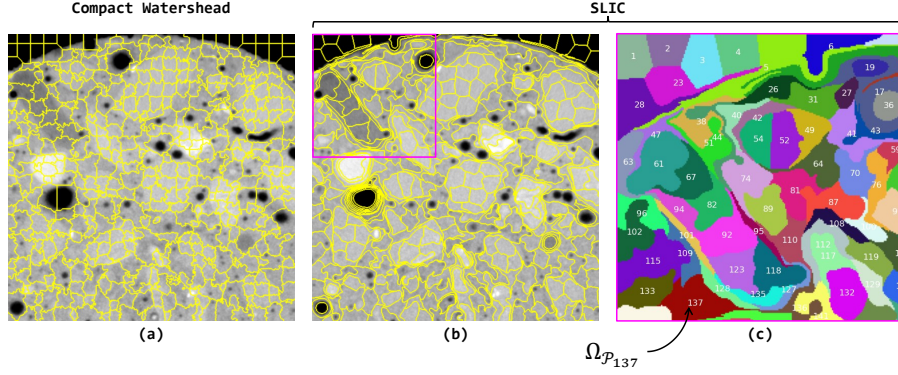


Figure 14: Comparison of superpixels obtained using *Scikit Image* [74] implementation of the compact watershed method [52] (a) and the SLIC algorithm [1] (b). These images are produced by overlaying the superpixel boundaries on the original grayscale image. Image (a) is composed of approximately 480 superpixels, while image (b) is composed of approximately 370 superpixels. In (c) the superpixel map is illustrated for the region inside the magenta box in (b). Each $\Omega_{\mathcal{P}_i}$ indicates to the location of a given superpixel.

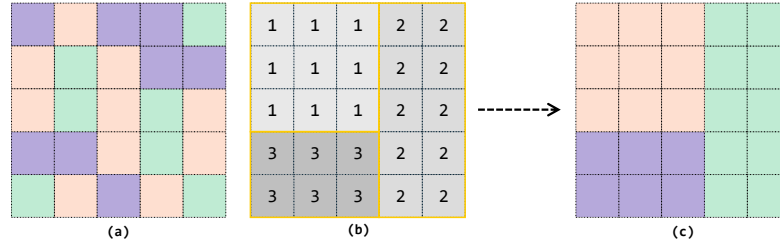


Figure 15: A schematic depiction of the superpixel refinement operation. Given an image with categorical pixels as in (a), depicted using colours and given a superpixel map as depicted (b) with number indicating the superpixel index, superpixel refinement function assigns to the region occupied by each superpixel the most frequently occurring categorical class in (a), which results in the output depicted in (c).

predicted using the model \mathcal{U}_{θ_t} is the most likely semantic category of all the pixels within that superpixel. And correspondingly, a label is generated by assigning to all locations in $\Omega_{\mathcal{P}_i}$ this class label, see Figure 15.

Nevertheless, components of $\hat{\mathbf{Y}}_t$ have no bounds over their relative magnitudes across the feature dimensions, which is otherwise enforced using (9) in a supervised training scenario. As such, under the aforementioned assumptions, it is possible for the model to collapse to a trivial solution where one of the channels has systematically higher or lower values compared to the others. This can result in solutions where the segmentation consists of only one phase. To counter this, the components of $\hat{\mathbf{Y}}_t$ are first normalized per feature dimension to obtain $\bar{\mathbf{Y}}_t = (\bar{y}_{h,w,f}^t) \in \mathbb{R}^{H \times W \times |\mathcal{C}|}$ with

$$\bar{y}_{h,w,f}^t = \frac{\hat{y}_{h,w,f}^t - \hat{\mu}_f^t}{\hat{\sigma}_f^t} \quad (10)$$

where, $\hat{\mu}_f^t$ and $\hat{\sigma}_f^t$ denote the mean and variance respectively, of elements of $\hat{\mathbf{Y}}_t$ for the f -th feature dimension, computed as

$$\hat{\mu}_f^t = \frac{1}{HW} \sum_{h=1}^H \sum_{w=1}^W \hat{y}_{h,w,f}^t,$$

$$(\hat{\sigma}_f^t)^2 = \frac{1}{HW} \sum_{h=1}^H \sum_{w=1}^W (\hat{y}_{h,w,f}^t - \hat{\mu}_f^t)^2.$$

$\bar{\mathbf{Y}}_t$ has components in each channel with zero mean and unit standard deviation, thereby, allowing each

feature dimension to have similar chance of being selected using $\arg \max$ classification.

However, the normalization in (10) also results in degradation of the output in certain circumstances. This is particularly evident in cases of class imbalance in images, i.e. instances where particular classes are absent or are not sufficiently represented. This adjustment then artificially translates and rescales the values in the channel corresponding to those classes in order to raise their chances of getting selected even though those classes are absent. Nevertheless, in the absence of this adjustment, the model collapses to produce less than the required number of phases. We note that this is an aspect that requires further studies.

Following this, for each location (h, w) the task of assigning a unique class label to each pixel is undertaken using $\arg \max$ label assignment operation such that $\bar{\mathbf{Y}}_t \xrightarrow{\arg \max} \hat{\mathbf{S}}_t$, where $\hat{\mathbf{S}}_t = (\hat{s}_{h,w}^t) \in \mathcal{C}^{H \times W}$ is the tensor of assigned pixel-wise labels such that

$$\hat{s}_{h,w}^t = \arg \max_{f \in \{1, \dots, |\mathcal{C}|\}} (\bar{y}_{h,w,f}^t). \quad (11)$$

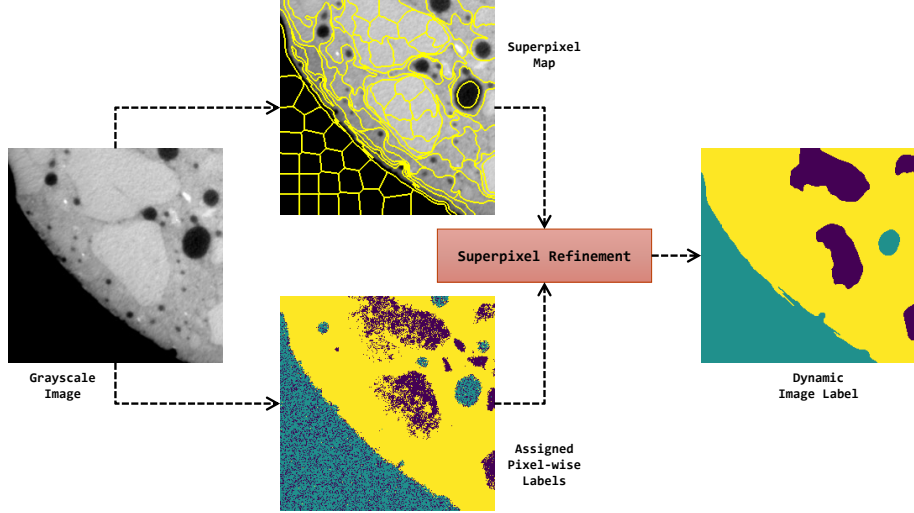


Figure 16: Superpixel refinement as part of the overall scheme. Given an image, the superpixel map is computed and for each training iteration, the assigned pixel-wise labels are refined to produce dynamic image labels.

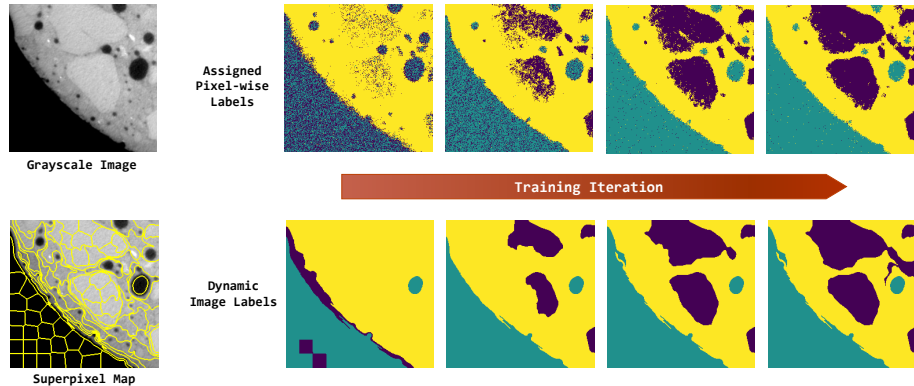


Figure 17: Illustration of evolution of dynamic image labels with respect to training iterations (Note: Number of images do not equate to the number of training iterations).

Finally, the constraint on spatial contiguity is enforced by what is referred to as *superpixel refinement* that automates the annotation process by converting the tensor of assigned pixel-wise labels to regional annotations. For this purpose, the tensor $\tilde{\mathbf{L}}_t = (\tilde{l}_{h,w}^t) \in \mathcal{C}^{H \times W}$ is introduced, which is referred to as the *dynamic image label* and evolves with every training iteration t . Given a spatial region $\Omega_{\mathcal{P}_i}$ of an image occupied by superpixel \mathcal{P}_i , the most frequently occurring label in the corresponding spatial region in $\hat{\mathbf{S}}_t$

is given as

$\tilde{l}_{h,w}^t = \text{mode}(\{\hat{s}_{h,w}^t\}) \forall (h, w) \in \Omega_{\mathcal{P}_i}$. The dynamic image label $\tilde{\mathbf{L}}_t$ is updated after every training iteration t . This process is schematically illustrated in Figure 16 as a part of the training workflow and its evolution with training progression is presented in Figure 17.

Therefore, at any iteration t , given the mapping $\mathbf{I} \xrightarrow{U_{\theta_t}} \hat{\mathbf{Y}}_t$, its normalization $\bar{\mathbf{Y}}_t = (\bar{y}_{h,w,f}^t) \in \mathbb{R}^{H \times W \times |\mathcal{C}|}$ and a dynamic label $\tilde{\mathbf{L}}_t$ with its one-hot encoding $\tilde{\mathbf{Y}}_t^{01} = (\tilde{y}_{h,w,f}^t) \in \{0, 1\}$, the cross-entropy in (9) is rewritten as

$$\tilde{\mathcal{L}}_{\text{CE}}^t = - \sum_{h=1}^H \sum_{w=1}^W \sum_{f=1}^{|\mathcal{C}|} \log \left(\frac{\exp(\bar{y}_{h,w,f}^t)}{\sum_{f=1}^{|\mathcal{C}|} \exp(\bar{y}_{h,w,f}^t)} \right) \tilde{y}_{h,w,f}^t \quad (12)$$

where, $\tilde{y}_{h,w,f}^t$ is iteration dependent. In fact for any $\mathbf{F}^{(h,w)}$, $\tilde{y}_{h,w,f}^t$ is not unique but may take any of the values in \mathcal{C} during training (see Figure 17). Training a model in such a situation is termed as unsupervised segmentation and the model is expected to gradually converge to produce the correct label.

It is important to note that in practice, training over the entire dataset is performed by traversing over it in small non-overlapping subsets called *mini-batches*, comprising multiple images, and the model weights are updated for every such subset, a process which is also termed as mini-batch learning. In this setting, the loss used for gradient computation is a cumulative metric, typically the sum or average over the individual losses computed for all images in a mini-batch. For more information on the reasoning behind the use of mini-batch for training, one may refer to [9, 4, 35, 66, 5]. Hence, in this work, the model parameters are updated using the gradient computed on the average loss over a set of images in a minibatch $\text{Avg}(\tilde{\mathcal{L}}_{\text{CE}}^t)_{\text{MB}}$ with respect to θ_t

$$\theta_{t+1} \leftarrow \theta_t - \eta \frac{\partial \text{Avg}(\tilde{\mathcal{L}}_{\text{CE}}^t)_{\text{MB}}}{\partial \theta_t}. \quad (13)$$

4. Implementation

4.1. Training, Validation and Test Datasets

Due to limitations on GPU memory, training was performed using tiles measuring 256×256 pixels that were cropped out of images measuring 1024×1024 pixels using the tiling strategy presented in Figure 18. The alternative approach of rescaling the images to a smaller dimension instead of tiling was not used since *Interfacial Transition Zone* (ITZ) are of particular importance in concretes, and doing so would have resulted in loss of detail.

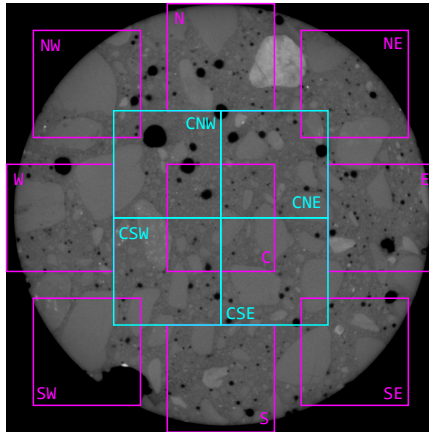


Figure 18: Tiling strategy used for generating training data. Each image yielded 13 tiles. The squares represent tile placement. Abbreviations - N: North, S: South, E: East, W: West, C: Center. Colours for representation purposes only. The squares at the four corners were placed 128 pixels away from the edges in each direction.

For training, a subset comprising approximately 9500 ($= D_{train}$) randomly chosen tiles obtained from approximately 1470 images belonging to 6 distinct XCT samples were used, representing approximately 41% of the available data in terms of pixels. A separate subset of approximately 4730 ($= D_{val}$) identically sized tiles was used for formulating a stopping criterion for the training process, and is hence termed as the validation dataset. These were also randomly chosen and it was ensured that there was no overlap between these two datasets.

Subsequently for each tile in both the datasets, a superpixel map was computed which remained fixed through all iterations. As already stated in the previous section, superpixels were generated using the algorithm termed as SLIC (Simple Linear Iterative Clustering) [1]. This algorithm when used on grayscale images is parameterized by three degrees of freedom, i.e, two for spatial proximity and one for pixel intensity and primarily requires two user-defined inputs, namely, the desired number of superpixels and the compactness parameter. The number of superpixels in an image also determines their size, while compactness controls, in simple terms, how square the ensuing superpixels are. In our case, the number of superpixels was chosen based on the fact that, for concretes, aggregates smaller than 4 mm are typically considered part of the mortar [58]. Therefore, this parameter was set to ensure that the superpixels were approximately 4mm equivalent in dimension. The compactness value was chosen through experimental trials to ensure that the superpixel boundaries adhered well to the phase boundaries in most cases and were not too sensitive to image noise, which otherwise resulted in jagged boundaries.

For evaluating the performance of the model on unseen data, a separate XCT-sample, distinct from the 6 XCT samples stated above, was used. This is the test dataset in this case and comprises approximately 590 slices measuring 1024×1024 pixels. This sample was preprocessed identically to the rest of the samples and no part of it was previously used for training or validation. This sample is hereon referred to as $\mathbf{T}_{PR} = \{\mathbf{I}_n^{PR}\}$. In the subsequent text the index n , corresponding to the slice index, has been omitted for visual clarity.

4.2. Training Procedure

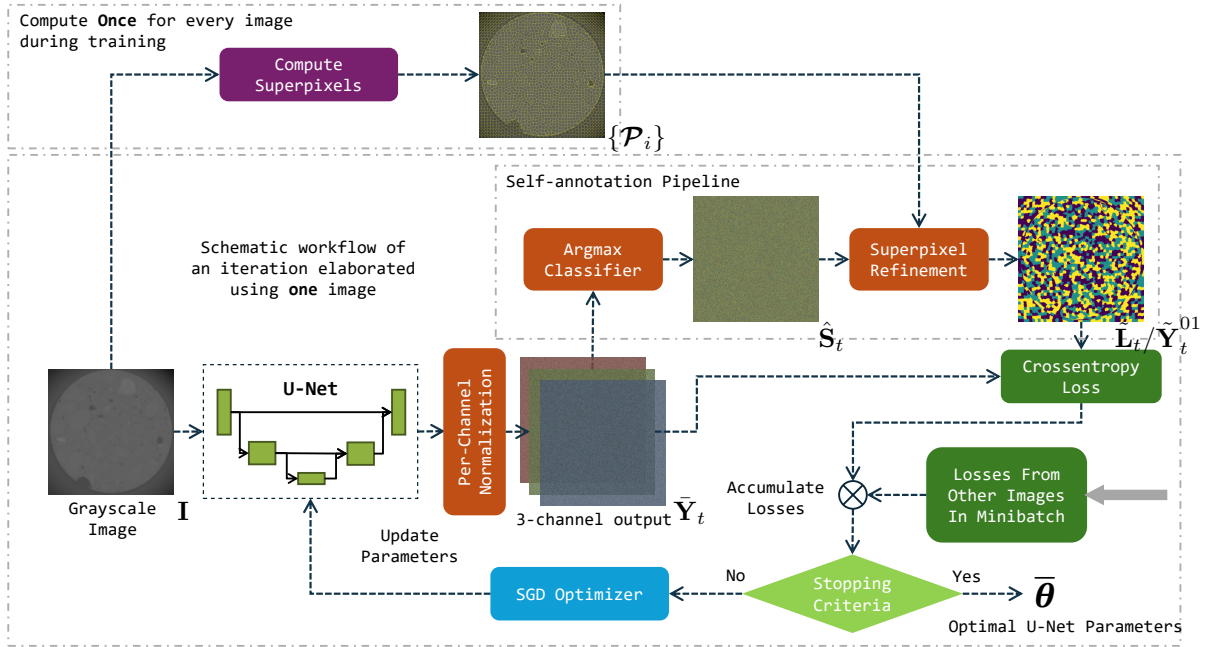


Figure 19: Schematic flowchart for unsupervised training of the U-Net model aided by dynamic label generation assuming a 3-channel output for one image. Superpixels for each image is computed once. Training is performed by iterating over the images several times. The output produced by the model is used to generate dynamic image labels. Each output channel corresponds to each material phase of interest, i.e. aggregate, mortar and concrete.

For training, the scheme presented in Figure 19 was followed. At each training iteration, for every input image (here tile), the model output was normalized per-channel and passed through the *self-*

annotation pipeline to produce a dynamic image label $\tilde{\mathbf{L}}_t$. The cross-entropy loss was then computed between the normalized model output $\bar{\mathbf{Y}}_t$ and one-hot encoded dynamic image label $\tilde{\mathbf{Y}}_t^{01}$ using (12). As already mentioned, since training was performed using minibatches, the model parameters were updated based on the average loss per minibatch $\text{Avg}(\mathcal{L}_{\text{CE}}^t)_{\text{MB}}$ using (13). Here, we would also like to clarify that training involves multiple passes over the entire dataset, wherein, during each pass, the model parameters are updated multiple times, i.e. once per minibatch. Therefore, a single pass over the dataset is referred to as an *epoch* (e), an update cycle per minibatch is referred to as an *iteration* (t). Since, here, training dataset size was $D_{\text{train}} = 9500$ tiles and minibatch size was $N = 24$ tiles, each epoch comprised $t_e = 396$ iterations where, $t_e = \lfloor \frac{D_{\text{train}}}{N} \rfloor + \iota$ with $\iota = 1$ if $(D_{\text{train}} \bmod N) \neq 0$ else $\iota = 0$.

Although the choice of using smaller tiles instead of full slices was guided by limitations on GPU memory, it was also noted that using smaller minibatches composed of entire images instead of using larger minibatches composed of tiles resulted in severe under-segmentation. Here, we define *under-segmentation* as a situation where the model fails to recognize all the phases present in an image, which results in segmentations with less than the required number of phases. In our case, it was primarily restricted to the aggregates and mortars being classified as the same phase.

The set of model parameters at $t = 0$ i.e. θ_0 was initialized following the Xavier-normal (also known as Glorot-normal) initialization method [21] for the kernels while the bias terms were initialized to zero. This was optimized using stochastic gradient descent (SGD) with an additional momentum parameter [69], where the gradient at iterations $t = 2, 3, \dots$ are updated by adding a weighted contribution of the gradient from iteration $t - 1$, except at iteration $t = 1$. This weighting factor is referred to as the momentum. An initial learning rate of $\eta = 0.0005$ with optimizer momentum 0.5 was used. The learning rate was adjusted during training through the use of *cosine annealing* with restarts [47]. The first restart interval was set to 10 epochs and doubled for each subsequent restart. The minimum learning rate was set to $\eta_{\text{min}} = 0.0001$.

Training performance was tracked at every epoch e by observing the evolution of mean $\mathcal{L}_{\text{CE}}^e$ over the entire validation dataset using the model parameters θ_e obtained at the end of the stated epoch. During validation, the model is run in prediction mode and therefore the dropout layers are deactivated and consequently, the mean validation losses are consistently lower than training losses. Trainings were run for $e_{\text{max}} = 100$ epochs, and following the usual practice, the set of model parameters for final prediction was chosen at the end of the epoch with minimum mean loss (at $e < e_{\text{max}}$ in all cases) on this dataset, which was the *stopping criterion*, yielding $\hat{\theta} = \theta_e$. This was done to ensure that the model did not overfit to the training data, where, increase in validation loss can be imagined as the tensor of assigned pixel-wise labels $\hat{\mathbf{S}}_t$ getting noisier as the model starts overfitting with further training.

4.3. Prediction Procedure

Due to the model \mathcal{U} being trained on tiles of size 256×256 pixels which were cropped out of the images, the model performed optimally when the prediction was obtained using similarly sized tiles cropped out of each \mathbf{I}^{PR} . Such a behaviour, where semantic segmentation models perform distinctly based on the size of the input image is well established [84]. However, stitching them together to reconstruct the full-size images also resulted in undesirable artifacts and discontinuities in prediction values at tile edges, which necessitated certain corrective measures such as overlapping at the edges during prediction. Nevertheless, it is presumed that training on large minibatches of full-sized images can effectively avoid such artifacts.

The entire framework was implemented using *Pytorch* [54] deep learning library. On a workstation equipped with AMD Ryzen-9 7950X with 128GB system memory and one Nvidia RTX4090 GPU with 24GB VRAM, training took approximately 3-4 min per epoch (i.e approx. 5-7h for the entire training process) and prediction for \mathbf{T}_{PR} required approximately 1-2 min. However it is to be noted that these times include certain overheads that were suboptimally implemented and performance may improve with an optimized code.

5. Experiments

Numerical experiments were first performed in a fully unsupervised manner where the model was trained by constraining it to produce three channels at the output corresponding to three distinct phases (US3). In this case it was found that the model consistently failed to unambiguously detect the porous

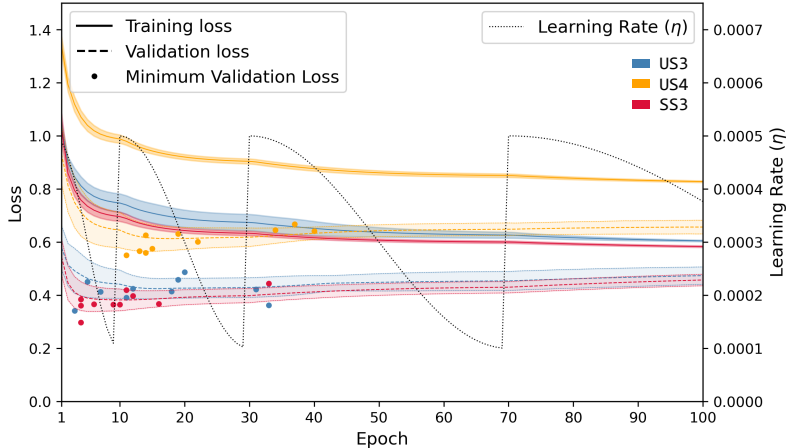


Figure 20: Mean training losses and mean validation losses averaged over 10-training runs for each case represented using solid and dashed line respectively. The standard deviation over the 10-runs is represented using the coloured region around the mean losses. Dotted black line indicates learning rate. The minimum validation loss for each experiment is marked using a dot.

phase in the images. Hence, the unsupervised training was repeated by relaxing the constraint on the output channels to four instead (US4). The two unsupervised cases are presented in Sections 5.1 and 5.2 respectively.

Since the porous phase was easily discernible and therefore could be segmented using simple thresholding, we further tested a semi-supervised training method. In which case, the model was constrained to produce three output channels (SS3). In this case, self-annotation was only performed for the aggregates and the mortar, while labels of the porous regions were pre-specified using labels obtained by thresholding. This case is presented in Section 5.3.

For each case, the 10 distinct models were trained using identical parameters, the average of the mean training and validation losses for each is presented in Figure 20. It was observed that although the evolution of losses followed similar pattern, there was considerable discrepancy in the epoch at which the minimum validation loss was observed. Nevertheless, the prediction outcomes were qualitatively similar and replicable among distinct training runs in all the cases. Since in practice, it can only be expected to run the training once, in the subsequent sections, we therefore only present an example of results that can be expected without any reference to a specific training run or to the epoch at which minimum mean loss on the validation dataset was observed.

For this, some changes in notation is introduced, whereby, while referring exclusively to the results in each of the cases, we omit any reference to epoch e and iteration t for reasons stated above and only refer to the cases using a subscript in each symbol. Otherwise, the symbols retain identical meaning as in Section 3.

5.1. Unsupervised Training: Given 3-phases (US3)

The model was first constrained to produce output comprising 3-feature channels, one for each material phase under consideration, and the self-annotation procedure was expected to generate labels for each of the 3 material phases. In the normalized prediction result $\hat{\mathbf{Y}}_{\text{US3}}^{\text{PR}}$ comprising 3 feature channels, examples of which for two slices are presented in Figure 21, it was observed that the model is able to assign one channel each to the aggregates and the mortar phase. However, it did not assign the third channel exclusively to the porous phase and instead, generated similar prediction values for both the aggregates and mortar phases, leading to ambiguity in its semantic meaning. This is particularly pronounced in case of bright aggregates, for which the model generated especially high values in this channel. This resulted in incorrect classification of certain aggregates in the pixel-wise assigned labels $\hat{\mathbf{S}}_{\text{US3}}^{\text{PR}}$ and the corresponding superpixel refinements $\hat{\mathbf{L}}_{\text{US3}}^{\text{PR}}$ examples of which are presented in Figure 22 for the same slices.

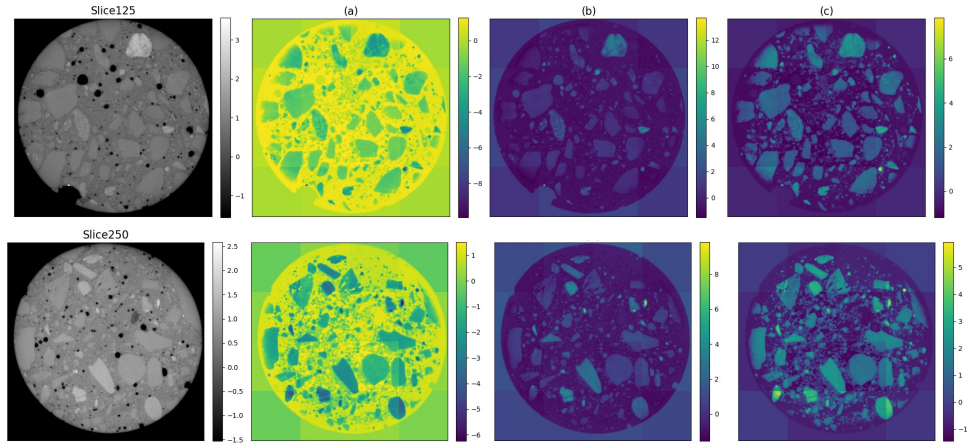


Figure 21: US3: Example of 3-channel prediction results using model trained in an unsupervised manner for the given input slices (left). Column (a) and (c) can be associated with the mortar and aggregate phases respectively. Channel (b) is ambiguous and displays similar scores for porosity and aggregates.

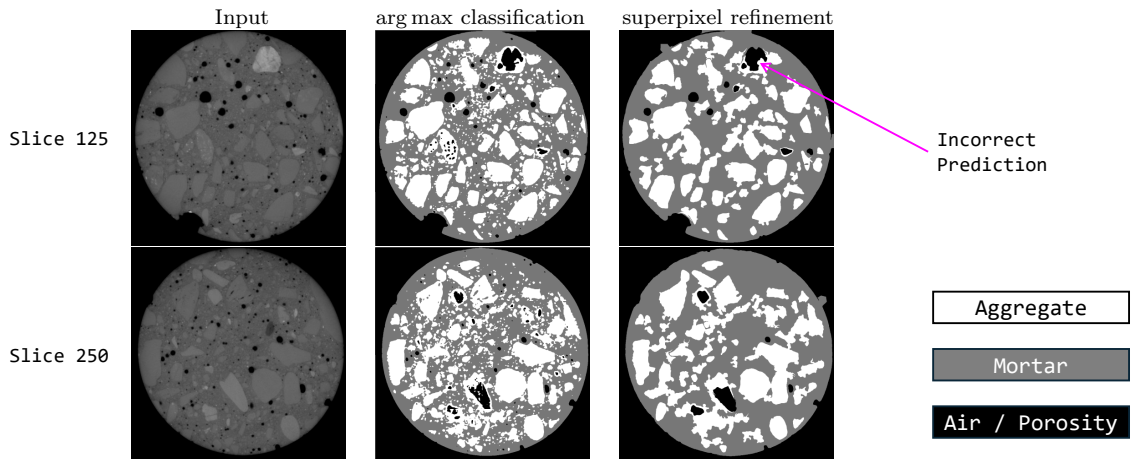


Figure 22: US3: arg max classification of \bar{Y}_{US3}^{PR} and the superpixel refinement \tilde{L}_{US3}^{PR} using parameters equivalent to that used during training.

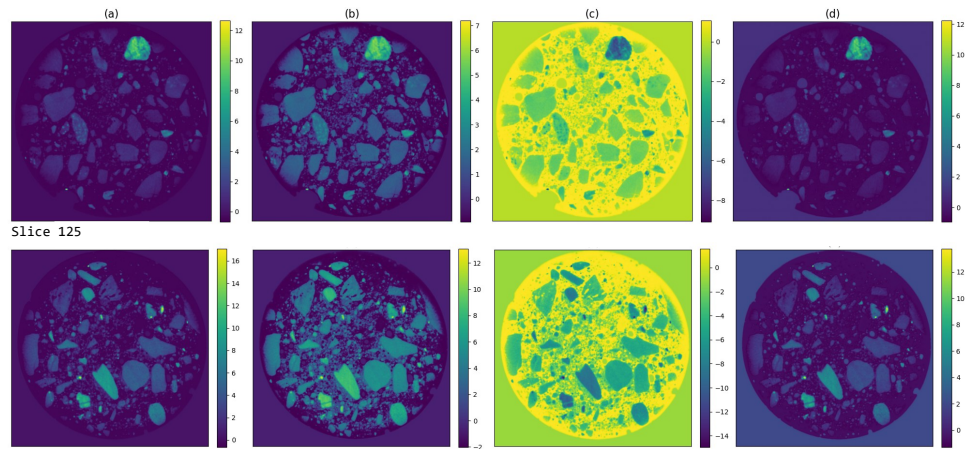


Figure 23: US4: Example of 4-channel prediction results using model trained in the unsupervised scenario for input slices presented in Figure 21 (left). Column (a) and (b) are associated with the aggregate phase, (c) is associated with the mortar phase. Column (d) is ambiguous with similar scores for porosity and aggregates.

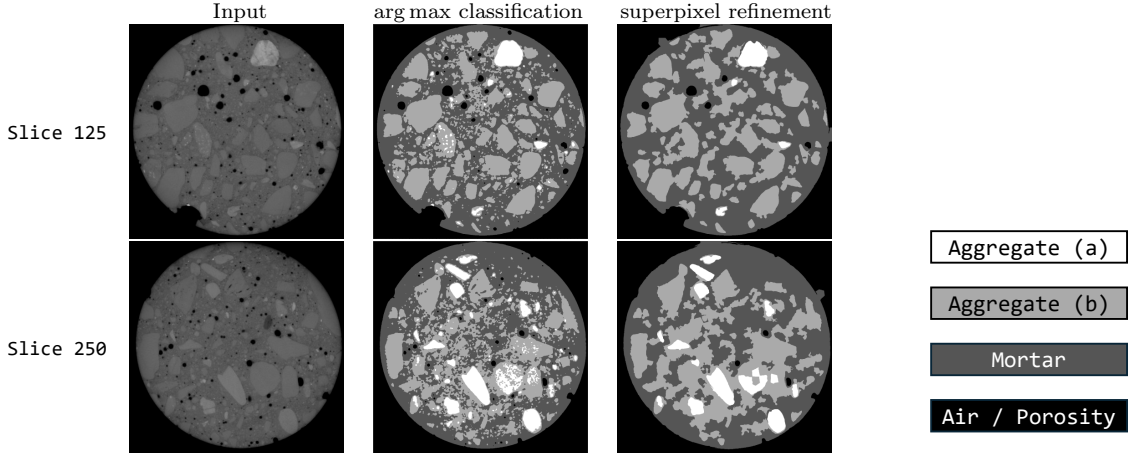


Figure 24: US4: arg max classification of $\bar{\mathbf{Y}}_{\text{US4}}^{\text{PR}}$ and the superpixel refinement $\tilde{\mathbf{L}}_{\text{US4}}^{\text{PR}}$ using parameters equivalent to that used during training.

5.2. Unsupervised Training: Given 4-phases (US4)

The constraint on the number of output features was relaxed to 4 to investigate if it had any ameliorative effect on the ambiguous classification of porosity and aggregates. The remainder of the training and prediction procedure is unchanged. However, now the self-annotation procedure was expected to generate 4-distinct labels, which is more than the number of material phases. Example of $\bar{\mathbf{Y}}_{\text{US4}}^{\text{PR}}$ for identical slices presented in Figure 21 (left) are presented in Figure 23. The model is able to unambiguously assign channels in $\bar{\mathbf{Y}}_{\text{US4}}^{\text{PR}}$ to the aggregate and the mortar phases. Moreover, the model also assigns an additional channel to the aggregate phase, but it remains unable to unambiguously assign the remaining feature channel exclusively to the porous phase and as before generates similar scores for the aggregates and the porosity.

The resulting $\hat{\mathbf{S}}_{\text{US4}}^{\text{PR}}$ for arg max over all the 4-channels is presented in Figure 24 alongside its superpixel-refinement $\tilde{\mathbf{L}}_{\text{US4}}^{\text{PR}}$ for two slices. When $\hat{\mathbf{S}}_{\text{US4}}^{\text{PR}}$ was generated by suppressing the aggregate channel (a), incorrect classification was observed for some particularly bright aggregates as the porous phase, similar to the previous case. In that respect, aggregate channel (a) seems to have a corrective effect and counteracts the incorrect classification of the ambiguous channel. Nevertheless, aggregate channel (b) continues to dominate the remaining aggregates and also results in incorrect classification of mortars as aggregates, particularly evident in regions with high concentration of small aggregates.

5.3. Semi-supervised Training: Given 3-phases (SS3)

Due to the limitations associated with the first two unsupervised cases involving ambiguity in identification of porosity, and considering that the porous phase in the XCT data is easy to resolve and segment using thresholding, experiments were also carried out in a semi-supervised manner whereby, the self-annotation procedure was modified to only label regions corresponding to the aggregate and the mortar phases while the regions occupied by the porous phase was annotated using the thresholded data. Given how well the intensities of the porous and non-porous regions are separated in the original XCT images, there are multiple thresholds at which almost identical results can be obtained, hence, specific details pertaining to thresholding are not presented here.

For the semi-supervised training, the model was constrained to produce 3 feature channels at the output. At each iteration t and for each image, the self-annotation procedure was first performed over two of the three output channels of $\bar{\mathbf{Y}}_t$, which were pre-assigned to the aggregate and the mortar phases. This led to an intermediate binary dynamic label for the aggregates and mortar phases and included incorrectly labeled regions supposed to be associated with the porous phase. The label for the porous regions was subsequently corrected by assigning the corresponding label to those region to attain the final 3-class label $\tilde{\mathbf{L}}_t$ consisting of both automatically labeled regions and regions with predefined labels. No other changes to the remainder of the training and prediction procedure were made. Hence, the

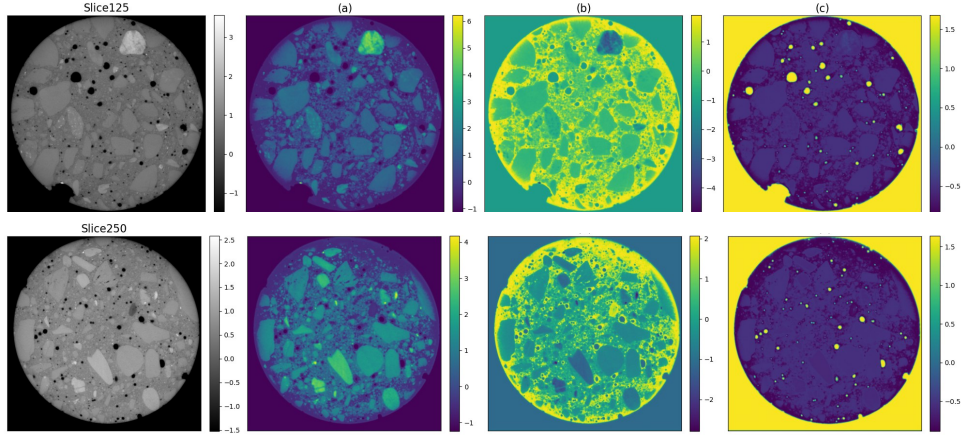


Figure 25: SS3: Example of 3-channel prediction results using the model trained in the semi-supervised manner for the given input slices (left). Column (a), (b) and (c) can unambiguously be associated with the aggregate, mortar and porosity respectively.

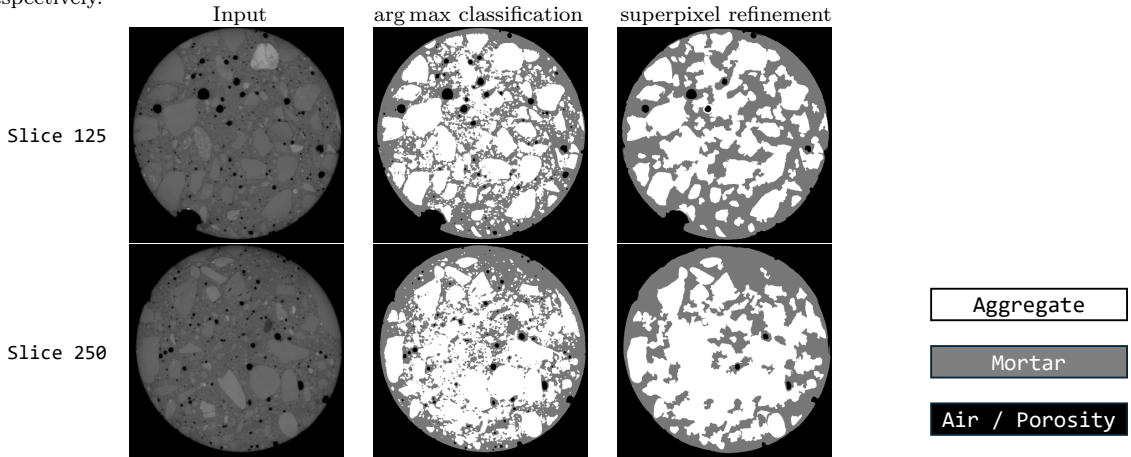


Figure 26: SS3: arg max classification of \bar{Y}_{SS3}^{PR} and the superpixel refinement using parameters equivalent to that used during training.

superpixel refinements in this case is not identical to the tensor \tilde{L}_t in Section 3 due to difference in the annotation procedure.

Normalized model prediction \bar{Y}_{SS3}^{PR} was obtained comprising 3 feature channels, examples of which for two slices are presented in Figure 25. From the images, it is evident that the model is able to resolve all the three distinct phases and hence assign a channel to each of the individual phases. In Figure 26, \hat{S}_{SS3}^{PR} is presented for two slices alongside their superpixel refinement.

6. Postprocessing

As demonstrated in the previous section, both the semi-supervised and the unsupervised methods were able to train the model such that it was able to distinguish between aggregates and mortar, without requiring labeled data for these phases. Nevertheless, generation of final classification label remains a challenge since the outputs obtained after arg max classification using (11) of \bar{Y}_t is not necessarily optimal, hence some degree of postprocessing is required.

For postprocessing, a manual thresholding-based approach is employed for obtaining the final classification labels. In this case, each channel of the normalized model output is treated individually. Since in a 3-phase scenario, a single phase is complementary to the remaining two phases, it is possible to use this approach on two of the three phases while third phase can be assigned the regions in an image left

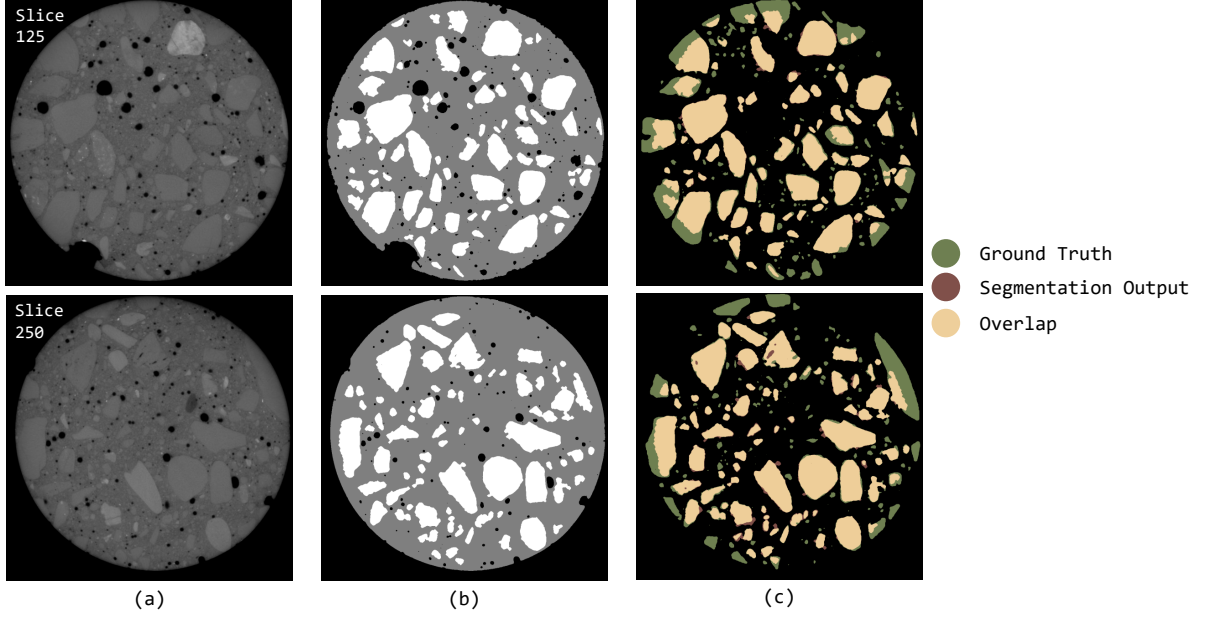


Figure 27: Original XCT slices from \mathbf{T}^{PR} (a). Example of 3-phase segmentation (b) using a thresholding-based postprocessing approach. Aggregates identified in white, mortar in gray and porosity in black. Comparison of Aggregates obtained following the process against ground truth labels for aggregates (c).

unoccupied by the other two phases. An example of this approach using $\bar{\mathbf{Y}}_{\text{SS3}}^{\text{PR}}$ for generation of the final labels is presented in Figure 27 where the channels corresponding to the porosity and aggregates were thresholded to generate a binary image for each phase and subsequently combined to produce three-phase images. Although, the threshold for each image is unique, for an entire sample, one may generate thresholds for a small set of slices at certain intervals of an XCT sample and subsequently use an interpolation algorithms, for example PCHIP Interpolator which is C1-smooth [18], to generate thresholds for the intermediate slices.

It is however to be noted that several sophisticated postprocessing techniques for semantic segmentation exist such as the use of conditional random fields [33], markov random fields [44], combination of global and local context of image regions [84] etc. Nevertheless, the postprocessing technique discussed in this work facilitates direct assessment of the current segmentation technique’s ability to distinguish between aggregates and mortar in concrete and therefore helps in establishing a baseline for subsequent improvements.

7. Results and Evaluation

For evaluating the final results \mathbf{T}_{PR} was used and 16-slices from it, taken at fixed intervals, were manually annotated and are henceforth referred to as the ground truth. The evaluation is only focused on the aggregates since mortar is complementary to it. $\bar{\mathbf{Y}}_{\text{SS3}}^{\text{PR}}$ was used since it is able to unambiguously assign a channel each to the given phases. The thresholding-based approach for postprocessing was used on the channel corresponding to the aggregate phase to obtain binary images consisting of only the aggregates. The resulting binary images of aggregates were further processed using a series of morphological operations to reduce noise and remove artifacts. Small holes up to 512 px in area were first filled, followed by binary erosion to eliminate narrow connections between large objects. Subsequently, objects smaller than 128 px in area were removed, and a final binary dilation was applied to restore areas lost during erosion. Furthermore, objects smaller than 256 px were also removed from the manually annotated (ground truth) images since they were too small to be considered part of the aggregate phase. For additional comparison, we also use examples of the aggregates obtained via direct manual thresholding of the XCT slices of \mathbf{T}^{PR} , which were processed by removing objects smaller than 128 px and removing holes smaller

than 256 px. In Figure 28, an example of the results obtained by thresholding \bar{Y}_{SS3}^{PR} is contrasted with the ground truth and the aggregates obtained by the direct thresholding of T^{PR} .

7.1. Qualitative Evaluation

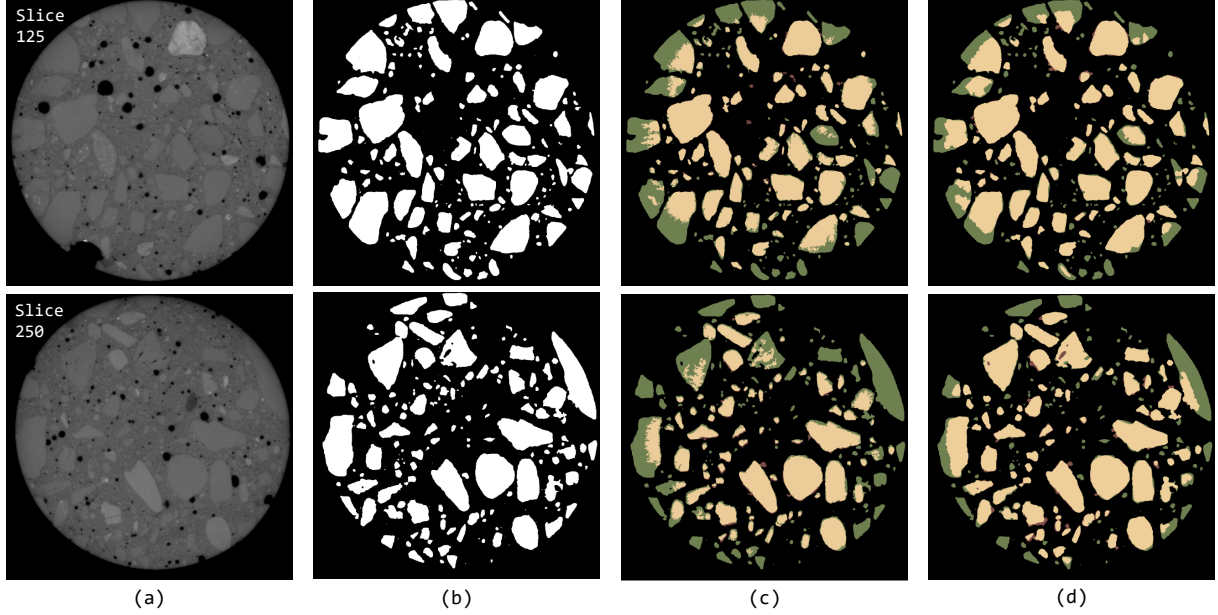


Figure 28: Comparison of binarized results of aggregates. (a) Input slices, (b) Ground Truth, (c) Aggregates obtained by direct manual thresholding of T^{PR} vs. Ground Truth, (d) Aggregates obtained by thresholding the aggregate-specific channel of \bar{Y}_{SS3}^{PR} vs. Ground Truth.

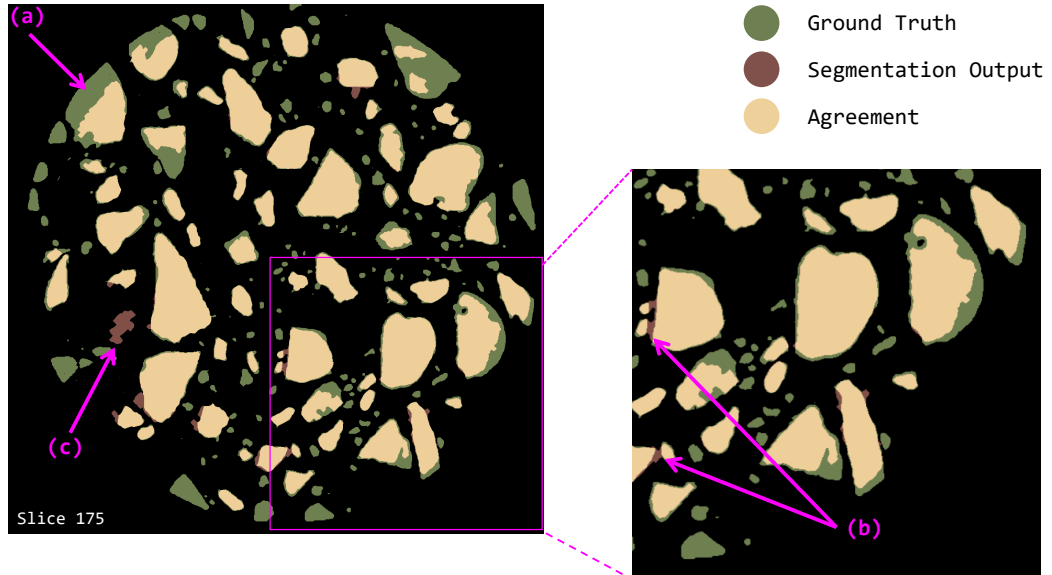


Figure 29: (a) Model fails to identify aggregates at the periphery of the cylindrical casting. (b) In case of aggregates located in close proximity, the model fails to effectively demarcate the boundaries between such aggregates. (c) A number of small aggregates clumped together to form incorrectly labeled aggregates.

From Figure 28, it is evident that the segmentation model produces better results when compared to direct thresholding of XCT samples. However, on a qualitative standpoint a few limitations were

also observed as shown in Figure 29 for a single slice against the ground truth. It was observed that the model performs well in identifying most of the aggregates, however, it consistently fails to detect aggregates near the periphery of the cylinder across the entire sample, as indicated by (a) in Figure 29. We assume that the sharp drop in pixel values between the solid phase and the porous region at the periphery of the cylinder could be the primary source of this error considering (2) where a weighted summation of pixels are computed. However, verification of this requires further investigation. Moreover, throughout the sample, in cases where aggregates are in close proximity, the model fails to identify narrow gaps of mortar between aggregates as shown by (b) in Figure 29. This, as a consequent has the effect that in regions where a number of small aggregates are located in close proximity, which should generally be assigned to the mortar phase based on their size, the model essentially detects these aggregates and joins them to form large regions that are incorrectly classified as aggregate indicated by (c) in Figure 29.

7.2. Quantitative Evaluation

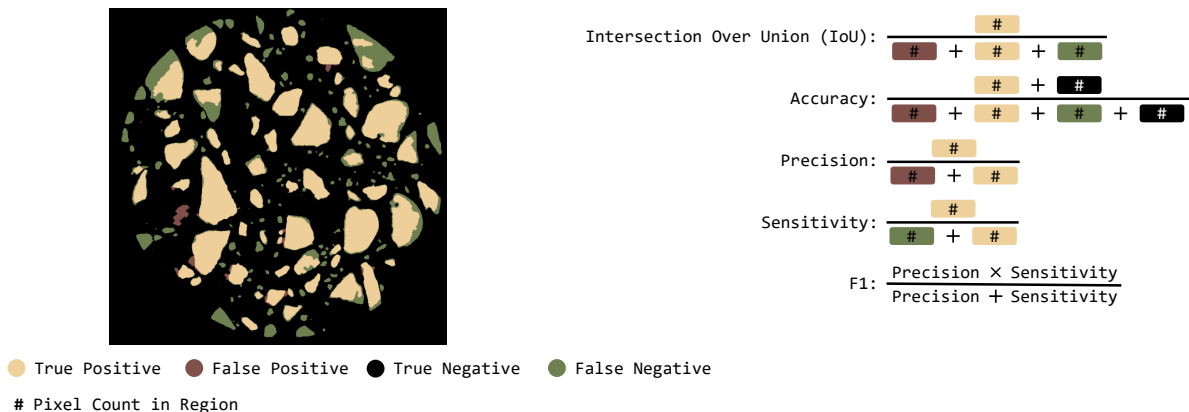


Figure 30: Interpretation of colours and definition of performance metrics.

Quantitative evaluation was carried out based on the metrics presented in Figure 30 against each of the 16 labeled slices of \mathbf{T}^{PR} focusing only on the aggregate phase. The results presented in Figure 31 consists of quantitative metrics for thresholding applied to the aggregate-specific channel of $\bar{\mathbf{Y}}_{\text{SS3}}^{\text{PR}}$ (logit thresholding) and to \mathbf{T}^{PR} (direct thresholding) and arg max classifications obtained directly from $\bar{\mathbf{Y}}_{\text{SS3}}^{\text{PR}}$. It is evident that thresholding applied to $\bar{\mathbf{Y}}_{\text{SS3}}^{\text{PR}}$ outperforms the other methods in most cases.

8. Conclusion

This work evaluates a CNN-based unsupervised semantic segmentation approach, focusing on low-contrast XCT scans of concrete. Challenges associated with XCT scans of concrete are briefly presented, including the lack of contrast between mortar and aggregates due to their similar X-ray attenuation coefficients, factors which collectively necessitate the use of a CNN-based semantic segmentation model for processing the XCT data for downstream applications. However, the unavailability of labeled training data poses a challenge for training a CNN-based deep learning model, making a self-annotation methodology necessary. The approach presented here enables the model to identify the prescribed phases without any labeled data enabling it to transform the bimodal pixel value distribution of the original grayscale XCT samples in a manner that improves discernibility between the aggregates and the mortar.

Certain limitations are also highlighted, including ambiguities in detecting the porous phase in a purely unsupervised setting, poor detection of aggregates near the periphery of the cylindrical samples and misclassification at regions with high concentration of small aggregates. Notably, it is highlighted that per-channel normalization of the model output is an aspect that requires further studies. While the U-Net model was fixed from the outset in this study, future studies may be conducted to examine whether smaller models can achieve satisfactory results for this specific application.

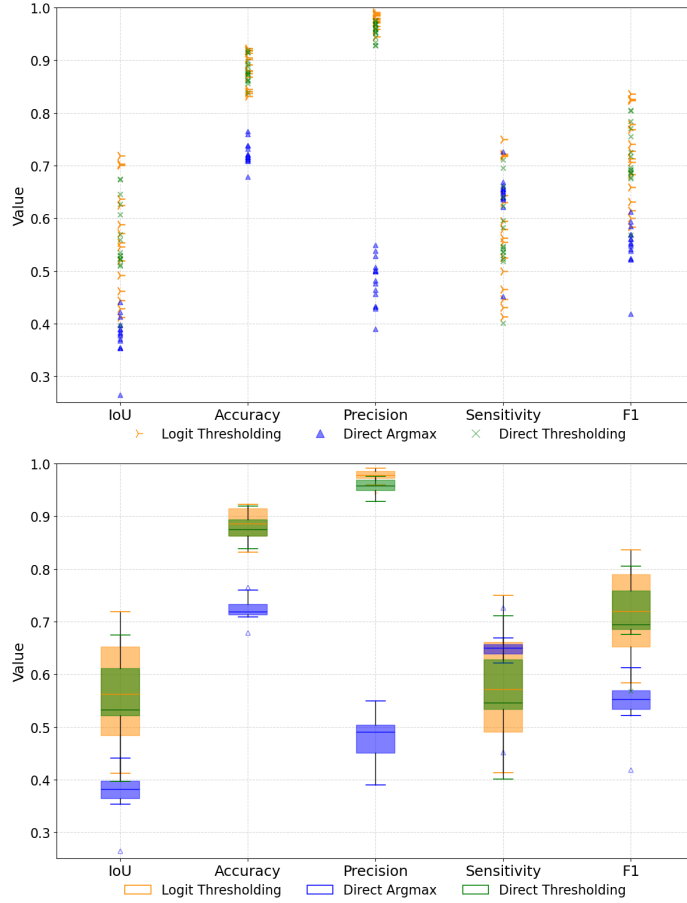


Figure 31: Quantitative evaluation of segmentation quality focusing on the aggregates compared to the ground truth of 16 slices using both postprocessing methods. Logit thresholding: thresholding applied to the aggregate-specific channel of $\hat{\mathbf{Y}}_{SS3}^{PR}$, Direct Thresholding: thresholding applied to \mathbf{T}^{PR} and Direct Argmax: aggregates extracted after arg max is applied to $\hat{\mathbf{Y}}_{SS3}^{PR}$.

Nevertheless, the methodology presented here was applied strictly in an unsupervised manner for the mortar and the aggregate phases and in its current state of development serves as an effective tool for enhancing XCT images to improve discernibility between aggregates and mortar. As such, it can be used for rapid generation of initial segmentation labels for subsequent supervised training of separate segmentation models or for fine-tuning an existing model on new concrete XCT datasets. Although this 2D a framework is employed here, extending it to a 3D framework should be straightforward.

We would also like to take this opportunity to inform readers about a recent trend toward the so-called *foundational models*, which are large, general-purpose models built for specific tasks such as image segmentation, with the *Segment Anything* (SA) models [39, 57] being a notable example. Such models can often be adapted for very specific tasks, for example, semantic segmentation in this case, through a *transfer learning* approach with minimal retraining. Nevertheless, SA models, for instance, are designed to operate on a wide variety of images and are trained on over 11 million colour images with more than 1 billion annotations. For specialized applications such as the segmentation of concrete XCTs, however, such models may not be computationally optimal, and satisfactory performance may still be achieved using smaller, purpose-built segmentation models.

Data Availability Statement

Processed datasets, software implementation and model weights are made available via Zenodo at <https://doi.org/10.5281/zenodo.18684512>.

CRedit Author Statement

KD: Conceptualization, Methodology, Software, Data Curation (Pre- and Post-processing), Investigation, Formal Analysis, Validation, Writing - Original Draft, Visualization; GR: Data Curation (XCT Scanning), Resources, Writing - Reviewing & Editing; JS: Conceptualization, Writing - Reviewing & Editing, Resources, Funding Acquisition; AK: Conceptualization, Methodology, Writing - Reviewing & Editing, Supervision, Funding Acquisition, Project Administration.

Acknowledgement

This work was developed within the bilateral SUMO project, funded by the Luxembourg National Research Fund (FNR) through the project INTER/GACR/21/16555380 and the Czech Science Foundation (GACR), project No. 22-35755K. KD additionally acknowledges financial support from the Student Grant Competition of the Czech Technical University in Prague, project No. SGS23/ 152/OHK1/3T/11. JS additionally acknowledges financial support from the European Union through the Operational Programme Jan Amos Komenský under project INODIN (CZ.02.01.01/00/23_020/0008487).

References

- [1] Achanta, R., Shaji, A., Smith, K., Lucchi, A., Fua, P., and Süsstrunk, S. (2010). Slic superpixels.
- [2] Bajcsy, P., Feldman, S., Majurski, M., Snyder, K., and Brady, M. (2020). Approaches to training multiclass semantic image segmentation of damage in concrete. *Journal of Microscopy*, 279(2):98–113.
- [3] Bangaru, S. S., Wang, C., Zhou, X., and Hassan, M. (2022). Scanning electron microscopy (sem) image segmentation for microstructure analysis of concrete using u-net convolutional neural network. *Automation in Construction*, 144:104602.
- [4] Bengio, Y. (2012). Practical recommendations for gradient-based training of deep architectures. In *Neural networks: Tricks of the trade: Second edition*, pages 437–478. Springer.
- [5] Bishop, C. M. and Bishop, H. (2023). *Deep learning: Foundations and concepts*. Springer Nature.
- [6] Bisschop, J. and van Mier, J. G. (2008). Effect of aggregates and microcracks on the drying rate of cementitious composites. *Cement and Concrete Research*, 38(10):1190–1196.
- [7] Böhm, R., Stiller, J., Behnisch, T., Zscheyge, M., Protz, R., Radloff, S., Gude, M., and Hufenbach, W. (2015). A quantitative comparison of the capabilities of in situ computed tomography and conventional computed tomography for damage analysis of composites. *Composites Science and Technology*, 110:62–68.
- [8] Bostanabad, R., Zhang, Y., Li, X., Kearney, T., Brinson, L. C., Apley, D. W., Liu, W. K., and Chen, W. (2018). Computational microstructure characterization and reconstruction: Review of the state-of-the-art techniques. *Progress in Materials Science*, 95:1–41.
- [9] Bottou, L. (2012). Stochastic gradient descent tricks. In *Neural networks: tricks of the trade: second edition*, pages 421–436. Springer.
- [10] Brisard, S., Serdar, M., and Monteiro, P. J. (2020). Multiscale x-ray tomography of cementitious materials: A review. *Cement and Concrete Research*, 128:105824.
- [11] Carrara, P., Kruse, R., Bentz, D. P., Lunardelli, M., Leusmann, T., Varady, P. A., and De Lorenzis, L. (2018). Improved mesoscale segmentation of concrete from 3d x-ray images using contrast enhancers. *Cement and Concrete Composites*, 93:30–42.
- [12] Chen, B., Zhang, H., Wang, G., Huo, J., Li, Y., and Li, L. (2023). Automatic concrete infrastructure crack semantic segmentation using deep learning. *Automation in Construction*, 152:104950.
- [13] Chen, L., Shan, W., and Liu, P. (2021). Identification of concrete aggregates using k-means clustering and level set method. In *Structures*, volume 34, pages 2069–2076. Elsevier.
- [14] Cheng, B., Schwing, A., and Kirillov, A. (2021). Per-pixel classification is not all you need for semantic segmentation. *Advances in neural information processing systems*, 34:17864–17875.
- [15] Coenen, M., Schack, T., Beyer, D., Heipke, C., and Haist, M. (2021). Semi-supervised segmentation of concrete aggregate using consensus regularisation and prior guidance. *ISPRS Annals of the Photogrammetry, Remote Sensing and Spatial Information Sciences V-2-2021 (2021)*, 2:83–91.
- [16] Curtarolo, S., Hart, G. L., Nardelli, M. B., Mingo, N., Sanvito, S., and Levy, O. (2013). The high-throughput highway to computational materials design. *Nature materials*, 12(3):191–201.
- [17] Dong, Y., Su, C., Qiao, P., and Sun, L. (2020). Microstructural crack segmentation of three-dimensional concrete images based on deep convolutional neural networks. *Construction and Building Materials*, 253:119185.
- [18] Fritsch, F. N. and Butland, J. (1984). A method for constructing local monotone piecewise cubic interpolants. *SIAM journal on scientific and statistical computing*, 5(2):300–304.

- [19] Fujiwara, T. (2008). Effect of aggregate on drying shrinkage of concrete. *Journal of Advanced Concrete Technology*, 6(1):31–44.
- [20] Fullwood, D. T., Niezgodá, S. R., Adams, B. L., and Kalidindi, S. R. (2010). Microstructure sensitive design for performance optimization. *Progress in Materials Science*, 55(6):477–562.
- [21] Glorot, X. and Bengio, Y. (2010). Understanding the difficulty of training deep feedforward neural networks. In *Proceedings of the thirteenth international conference on artificial intelligence and statistics*, pages 249–256. JMLR Workshop and Conference Proceedings.
- [22] Gonzalez, R. C. (2009). *Digital image processing*. Pearson education india.
- [23] Goodfellow, I., Bengio, Y., and Courville, A. (2016). *Deep Learning*. MIT Press. <http://www.deeplearningbook.org>.
- [24] Havlásek, P. and Jirásek, M. (2016). Multiscale modeling of drying shrinkage and creep of concrete. *Cement and concrete research*, 85:55–74.
- [25] Havlásek, P., Šmilauer, V., Dohnalová, L., and Sovják, R. (2021). Shrinkage-induced deformations and creep of structural concrete: 1-year measurements and numerical prediction. *Cement and Concrete Research*, 144:106402.
- [26] He, K., Gkioxari, G., Dollár, P., and Girshick, R. (2017). Mask r-cnn. In *Proceedings of the IEEE international conference on computer vision*, pages 2961–2969.
- [27] Hilloulin, B., Bekrine, I., Schmitt, E., and Loukili, A. (2022). Modular deep learning segmentation algorithm for concrete microscopic images. *Construction and Building Materials*, 349:128736.
- [28] Hufenbach, W., Böhm, R., Gude, M., Berthel, M., Hornig, A., Ručevskis, S., and Andrich, M. (2012). A test device for damage characterisation of composites based on in situ computed tomography. *Composites Science and Technology*, 72(12):1361–1367.
- [29] Idiart, A., Bisschop, J., Caballero, A., and Lura, P. (2012). A numerical and experimental study of aggregate-induced shrinkage cracking in cementitious composites. *Cement and Concrete Research*, 42(2):272–281.
- [30] Ioffe, S. and Szegedy, C. (2015). Batch normalization: Accelerating deep network training by reducing internal covariate shift. In *International conference on machine learning*, pages 448–456. pmlr.
- [31] Jung, C., Müsebeck, F., Barisin, T., Schladitz, K., Redenbach, C., Kiesche, M., and Pahn, M. (2022). Towards automatic crack segmentation in 3d concrete images. In *11th conf. ind. comput. tomogr.(ICT)*.
- [32] Kalidindi, S. R., Buzzy, M., Boyce, B. L., and Dingreville, R. (2022). Digital twins for materials. *Frontiers in Materials*, 9:818535.
- [33] Kamnitsas, K., Ledig, C., Newcombe, V. F., Simpson, J. P., Kane, A. D., Menon, D. K., Rueckert, D., and Glocker, B. (2017). Efficient multi-scale 3d cnn with fully connected crf for accurate brain lesion segmentation. *Medical image analysis*, 36:61–78.
- [34] Kanezaki, A. (2018). Unsupervised image segmentation by backpropagation. In *2018 IEEE international conference on acoustics, speech and signal processing (ICASSP)*, pages 1543–1547. IEEE.
- [35] Keskar, N. S., Mudigere, D., Nocedal, J., Smelyanskiy, M., and Tang, P. T. P. (2016). On large-batch training for deep learning: Generalization gap and sharp minima. *arXiv preprint arXiv:1609.04836*.
- [36] Kim, H.-T., Han, T.-S., Lee, Y. H., Park, K., et al. (2024). Recursive aggregate segmentation by erosion and reconstitution (raser) to characterize concrete microstructure using complementarity of x-ray and neutron computed tomography. *Cement and Concrete Composites*, 148:105437.

- [37] Kim, H.-T., Szilágyi, V., Kis, Z., Szentmiklósi, L., Glinicki, M. A., Park, K., et al. (2021). Reconstruction of concrete microstructure using complementarity of x-ray and neutron tomography. *Cement and Concrete Research*, 148:106540.
- [38] Kim, W., Kanazaki, A., and Tanaka, M. (2020). Unsupervised learning of image segmentation based on differentiable feature clustering. *IEEE Transactions on Image Processing*, 29:8055–8068.
- [39] Kirillov, A., Mintun, E., Ravi, N., Mao, H., Rolland, C., Gustafson, L., Xiao, T., Whitehead, S., Berg, A. C., Lo, W.-Y., et al. (2023). Segment anything. In *Proceedings of the IEEE/CVF International Conference on Computer Vision*, pages 4015–4026.
- [40] Kumar, P., Sharma, A., and Kota, S. R. (2021). Automatic multiclass instance segmentation of concrete damage using deep learning model. *IEEE Access*, 9:90330–90345.
- [41] Kumar, R. and Bhattacharjee, B. (2003). Porosity, pore size distribution and in situ strength of concrete. *Cement and concrete research*, 33(1):155–164.
- [42] LeCun, Y., Boser, B., Denker, J. S., Henderson, D., Howard, R. E., Hubbard, W., and Jackel, L. D. (1989). Backpropagation applied to handwritten zip code recognition. *Neural computation*, 1(4):541–551.
- [43] LeCun, Y., Bottou, L., Bengio, Y., and Haffner, P. (1998). Gradient-based learning applied to document recognition. *Proceedings of the IEEE*, 86(11):2278–2324.
- [44] Liu, Z., Li, X., Luo, P., Loy, C. C., and Tang, X. (2017). Deep learning markov random field for semantic segmentation. *IEEE transactions on pattern analysis and machine intelligence*, 40(8):1814–1828.
- [45] Loeffler, C. M., Qiu, Y., Martin, B., Heard, W., Williams, B., and Nie, X. (2018). Detection and segmentation of mechanical damage in concrete with x-ray microtomography. *Materials Characterization*, 142:515–522.
- [46] Lorenzoni, R., Curosu, I., Paciornik, S., Mechtcherine, V., Oppermann, M., and Silva, F. (2020). Semantic segmentation of the micro-structure of strain-hardening cement-based composites (shcc) by applying deep learning on micro-computed tomography scans. *Cement and Concrete Composites*, 108:103551.
- [47] Loshchilov, I. and Hutter, F. (2016). Sgdr: Stochastic gradient descent with warm restarts. *arXiv preprint arXiv:1608.03983*.
- [48] Meddah, M. S., Zitouni, S., and Belâabes, S. (2010). Effect of content and particle size distribution of coarse aggregate on the compressive strength of concrete. *Construction and building materials*, 24(4):505–512.
- [49] Miao, Y., Wang, H., Zhang, Y., Feng, T., Yali, L., Liqun, L., Lin, J., Zeyu, L., and Jiang, J. (2024). A numerical model for predicting the drying shrinkage behavior of concrete under ultra-low relative humidity. *Construction and Building Materials*, 411:134459.
- [50] Myong Lee, K., Buyukozturk, O., and Oumera, A. (1992). Fracture analysis of mortar-aggregate interfaces in concrete. *Journal of engineering mechanics*, 118(10):2031–2046.
- [51] Naresh, K., Khan, K., Umer, R., and Cantwell, W. J. (2020). The use of x-ray computed tomography for design and process modeling of aerospace composites: A review. *Materials & Design*, 190:108553.
- [52] Neubert, P. and Protzel, P. (2014). Compact watershed and preemptive slic: On improving trade-offs of superpixel segmentation algorithms. In *2014 22nd international conference on pattern recognition*, pages 996–1001. IEEE.
- [53] Niu, D., Wang, X., Han, X., Lian, L., Herzig, R., and Darrell, T. (2024). Unsupervised universal image segmentation. In *Proceedings of the IEEE/CVF Conference on Computer Vision and Pattern Recognition*, pages 22744–22754.

- [54] Paszke, A., Gross, S., Massa, F., Lerer, A., Bradbury, J., Chanan, G., Killeen, T., Lin, Z., Gimelshein, N., Antiga, L., et al. (2019). Pytorch: An imperative style, high-performance deep learning library. *Advances in neural information processing systems*, 32.
- [55] Pecha, M., Cermak, M., Hapla, V., Horak, D., and Tomcala, J. (2017). Advanced approach of material region detections on fibre-reinforced concrete ct-scans. *Advances in Electrical and Electronic Engineering*, 15(2):223–229.
- [56] Rao, G. A. and Raghu Prasad, B. (2004). Influence of type of aggregate and surface roughness on the interface fracture properties. *Materials and Structures*, 37:328–334.
- [57] Ravi, N., Gabeur, V., Hu, Y.-T., Hu, R., Ryali, C., Ma, T., Khedr, H., Rädle, R., Rolland, C., Gustafson, L., et al. (2024). Sam 2: Segment anything in images and videos. *arXiv preprint arXiv:2408.00714*.
- [58] Ren, Q., Pacheco, J., and de Brito, J. (2023). Methods for the modelling of concrete mesostructures: a critical review. *Construction and Building Materials*, 408:133570.
- [59] Ronneberger, O., Fischer, P., and Brox, T. (2015). U-net: Convolutional networks for biomedical image segmentation. In *Medical image computing and computer-assisted intervention–MICCAI 2015: 18th international conference, Munich, Germany, October 5–9, 2015, proceedings, part III 18*, pages 234–241. Springer.
- [60] Rumelhart, D. E., Hinton, G. E., and Williams, R. J. (1986). Learning representations by back-propagating errors. *nature*, 323(6088):533–536.
- [61] Saha, S. K., Pradhan, S., and Barai, S. V. (2020). Use of machine learning based technique to x-ray microtomographic images of concrete for phase segmentation at meso-scale. *Construction and Building Materials*, 249:118744.
- [62] Scrivener, K. L., Crumbie, A. K., and Laugesen, P. (2004). The interfacial transition zone (itz) between cement paste and aggregate in concrete. *Interface science*, 12(4):411–421.
- [63] Shi, M., Hua, T., Yang, Z. J., Tan, C., and Wen, Y. (2024). Weakly supervised deep learning-based concrete aggregates automatic segmentation for assessing separation degree. *Journal of Building Engineering*, 82:108342.
- [64] Siddique, N., Paheding, S., Elkin, C. P., and Devabhaktuni, V. (2021). U-net and its variants for medical image segmentation: A review of theory and applications. *Ieee Access*, 9:82031–82057.
- [65] Sleiman, H. C., Moreira, M. H., Tengattini, A., and Dal Pont, S. (2023). From tomographic imaging to numerical simulations: an open-source workflow for true morphology mesoscale fe meshes. *RILEM Technical Letters*, 8:158–164.
- [66] Smith, S., Elsen, E., and De, S. (2020). On the generalization benefit of noise in stochastic gradient descent. In *International Conference on Machine Learning*, pages 9058–9067. PMLR.
- [67] Srivastava, N., Hinton, G., Krizhevsky, A., Sutskever, I., and Salakhutdinov, R. (2014). Dropout: a simple way to prevent neural networks from overfitting. *The journal of machine learning research*, 15(1):1929–1958.
- [68] Stamati, O., Roubin, E., Andò, E., and Malecot, Y. (2018). Phase segmentation of concrete x-ray tomographic images at meso-scale: Validation with neutron tomography. *Cement and Concrete Composites*, 88:8–16.
- [69] Sutskever, I., Martens, J., Dahl, G., and Hinton, G. (2013). On the importance of initialization and momentum in deep learning. In *International conference on machine learning*, pages 1139–1147. PMLR.

- [70] Szegedy, C., Vanhoucke, V., Ioffe, S., Shlens, J., and Wojna, Z. (2016). Rethinking the inception architecture for computer vision. In *Proceedings of the IEEE conference on computer vision and pattern recognition*, pages 2818–2826.
- [71] Thakur, M. M., Enright, S., and Hurley, R. C. (2023). Phase segmentation in x-ray ct images of concrete with implications for mesoscale modeling. *Construction and Building Materials*, 403:133033.
- [72] Tian, W., Cheng, X., Liu, Q., Yu, C., Gao, F., and Chi, Y. (2021). Meso-structure segmentation of concrete ct image based on mask and regional convolution neural network. *Materials & Design*, 208:109919.
- [73] Tompson, J., Goroshin, R., Jain, A., LeCun, Y., and Bregler, C. (2015). Efficient object localization using convolutional networks. In *Proceedings of the IEEE conference on computer vision and pattern recognition*, pages 648–656.
- [74] Van der Walt, S., Schönberger, J. L., Nunez-Iglesias, J., Boulogne, F., Warner, J. D., Yager, N., Gouillart, E., and Yu, T. (2014). scikit-image: image processing in python. *PeerJ*, 2:e453.
- [75] Vásárhelyi, L., Kónya, Z., Kukovecz, Á., and Vajtai, R. (2020). Microcomputed tomography-based characterization of advanced materials: a review. *Materials Today Advances*, 8:100084.
- [76] Wang, W., Su, C., and Zhang, H. (2022). Automatic segmentation of concrete aggregate using convolutional neural network. *Automation in Construction*, 134:104106.
- [77] Wen, F., Li, W., Zhou, G., Li, H., Chen, T., and Zhang, K. (2024). A simplified numerical simulation of uniaxial compression for polyacrylonitrile fiber reinforced permeable concrete based on ct images. *Construction and Building Materials*, 411:134319.
- [78] Xia, X. and Kulis, B. (2017). W-net: A deep model for fully unsupervised image segmentation. *arXiv preprint arXiv:1711.08506*.
- [79] Yamane, T. and Chun, P.-j. (2020). Crack detection from a concrete surface image based on semantic segmentation using deep learning. *Journal of Advanced Concrete Technology*, 18(9):493–504.
- [80] Yang, Z., Ren, W., Sharma, R., McDonald, S., Mostafavi, M., Vertyagina, Y., and Marrow, T. (2017). In-situ x-ray computed tomography characterisation of 3d fracture evolution and image-based numerical homogenisation of concrete. *Cement and Concrete Composites*, 75:74–83.
- [81] Zeiler, M. D., Krishnan, D., Taylor, G. W., and Fergus, R. (2010). Deconvolutional networks. In *2010 IEEE Computer Society Conference on computer vision and pattern recognition*, pages 2528–2535. IEEE.
- [82] Zhang, P., Wittmann, F. H., Lura, P., Müller, H. S., Han, S., and Zhao, T. (2018). Application of neutron imaging to investigate fundamental aspects of durability of cement-based materials: A review. *Cement and Concrete Research*, 108:152–166.
- [83] Zhou, S.-B., Shen, A.-Q., and Li, G.-F. (2015). Concrete image segmentation based on multiscale mathematic morphology operators and otsu method. *Advances in Materials Science and Engineering*, 2015(1):208473.
- [84] Zhu, G., Wang, R., Liu, Y., Zhu, Z., Gao, C., Liu, L., and Sang, N. (2023). An adaptive post-processing network with the global-local aggregation for semantic segmentation. *IEEE Transactions on Circuits and Systems for Video Technology*.